The Astrophysical Journal, 908:19 (20pp), 2021 February 10 https://doi.org/10.3847/1538-4357/abd24d

Black Hole Mass Measurements of Radio Galaxies NGC 315 and NGC 4261 Using ALMA CO Observations*

Benjamin D. Boizelle[1,2], Jonelle L. Walsh[2], Aaron J. Barth[3], David A. Buote[3], Andrew J. Baker[4], Jeremy Darling[5], Luis C. Ho[6], Jonathan Cohn[2], and Kyle M. Kabasares[3]

[1] Department of Physics and Astronomy, N284 ESC, Brigham Young University, Provo, UT 84602, USA; boizellb@byu.edu
[2] George P. and Cynthia Woods Mitchell Institute for Fundamental Physics and Astronomy, 4242 TAMU, Texas A&M University, College Station, TX 77843-4242, USA
[3] Department of Physics and Astronomy, 4129 Frederick Reines Hall, University of California, Irvine, CA 92697-4575, USA
[4] Department of Physics and Astronomy, Rutgers, the State University of New Jersey, 136 Frelinghuysen Road, Piscataway, NJ 08854-8019, USA
[5] Center for Astrophysics and Space Astronomy, Department of Astrophysical and Planetary Sciences, University of Colorado, 389 UCB, Boulder, CO 80309-0389, USA
[6] Kavli Institute for Astronomy and Astrophysics, Peking University, Beijing 100871, China; Department of Astronomy, School of Physics, Peking University, Beijing 100871, People's Republic of China

Received 2020 October 8; revised 2020 December 7; accepted 2020 December 8; published 2021 February 9

Abstract

We present Atacama Large Millimeter/submillimeter Array (ALMA) Cycle 5 and Cycle 6 observations of CO (2−1) and CO (3−2) emission at 0.″2−0.″3 resolution in two radio-bright, brightest group/cluster early-type galaxies, NGC 315 and NGC 4261. The data resolve CO emission that extends within their black hole (BH) spheres of influence (r_g), tracing regular Keplerian rotation down to just tens of parsecs from the BHs. The projected molecular gas speeds in the highly inclined ($i \gtrsim 60°$) disks rise at least to 500 km s^{-1} near their galaxy centers. We fit dynamical models of thin-disk rotation directly to the ALMA data cubes and account for the extended stellar mass distributions by constructing galaxy surface brightness profiles corrected for a range of plausible dust extinction values. The best-fit models yield $(M_{BH}/10^9\,M_\odot) = 2.08 \pm 0.01(\mathrm{stat})^{+0.32}_{-0.14}(\mathrm{sys})$ for NGC 315 and $(M_{BH}/10^9\,M_\odot) = 1.67 \pm 0.10(\mathrm{stat})^{+0.39}_{-0.24}(\mathrm{sys})$ for NGC 4261, the latter of which is larger than previous estimates by a factor of ∼3. The BH masses are broadly consistent with the relations between BH masses and host galaxy properties. These are among the first ALMA observations to map dynamically cold gas kinematics well within the BH-dominated regions of radio galaxies, resolving the respective r_g by factors of ∼5−10. The observations demonstrate ALMA's ability to precisely measure BH masses in active galaxies, which will enable more confident probes of accretion physics for the most massive galaxies.

Unified Astronomy Thesaurus concepts: Supermassive black holes (1663); Fanaroff-Riley radio galaxies (526); Molecular gas (1073); Millimeter astronomy (1061); Submillimeter astronomy (1647); Galaxy kinematics (602); Astronomy data modeling (1859)

1. Introduction

At the center of presumably every large galaxy resides a supermassive black hole (BH), and dynamical measurements of the BH masses (M_{BH}) of over 100 galaxies have been made in the past two decades (e.g., Kormendy & Ho 2013; Saglia et al. 2016 and references therein). As a result, strong correlations have been established between the BH mass and several large-scale host galaxy properties, especially the stellar velocity dispersion ($\sigma_\star$; e.g., Ferrarese & Merritt 2000; Gebhardt et al. 2000) and the stellar bulge luminosity (L_{bul}; e.g., Kormendy & Richstone 1995) and mass (M_{bul}; e.g., McConnell & Ma 2013). These empirical relations suggest that the central BH and host galaxy grow in tandem through a series of accretion and merger events with feedback that regulates star formation.

The current data hint at a steeper $M_{BH}-\sigma_\star$ slope for the most luminous early-type galaxies (ETGs; see Bernardi et al. 2007; Lauer et al. 2007), which include several brightest group/cluster galaxies (BGGs/BCGs). One plausible explanation is that BH growth follows a different evolutionary track in merger-rich environments (see, e.g., Bogdán et al. 2018). However, the BH census remains incomplete above $\sim 10^9\,M_\odot$, and typical M_{BH} uncertainties are of order 25% in this high-mass regime (e.g., Saglia et al. 2016). In addition, potentially serious, and often unexplored, systematics in both stellar and gas-dynamical models may bias M_{BH} determinations (for a discussion, see Kormendy & Ho 2013). Any confident interpretation of BGG/BCG BH growth will require both larger numbers of M_{BH} measurements and greater measurement precision.

The most reliable BH mass measurements come from spatially resolved tracer kinematics that originate well within the sphere of influence ($r_g \approx GM_{BH}/\sigma_\star^2$). Within this radius, the BH's gravitational influence dominates over the galaxy's extended mass contributions. Circumnuclear gas disks have long been appealing kinematic targets for constraining BH masses because they are insensitive to large-scale galaxy properties, although high gas turbulence in many cases and potential noncircular motion have limited the usefulness of ionized gas tracers (Verdoes Kleijn et al. 2006). Molecular gas disks, likely to have significantly less turbulent motion, offer an attractive alternative to ionized gas. In addition, very long baseline interferometry of water megamaser disks reveals emission arising from very deep within r_g (e.g., Kuo et al. 2011; Zhao et al. 2018). However, megamaser disks are rare and tend to be found in late-type galaxies with $M_{BH} \sim 10^6-10^7$

* Based on observations made with the NASA/ESA Hubble Space Telescope, obtained at the Space Telescope Science Institute, which is operated by the Association of Universities for Research in Astronomy, Inc., under NASA contract NAS 5-26555. These observations are associated with programs #5124, 6673, 14219, and 15909.

$M_\odot$. Searches for maser emission in the most massive galaxies have so far been unsuccessful (van den Bosch et al. 2016). Davis et al. (2013) demonstrated that the more common tracer CO could be used to constrain BH masses in ETGs, and the increased sensitivity and angular resolution of the Atacama Large Millimeter/submillimeter Array (ALMA) relative to the previous generation of millimeter/submillimeter facilities have reinvigorated gas-dynamical efforts.

About 10% of all luminous ETGs exhibit morphologically round dust features in Hubble Space Telescope (HST) images (e.g., Lauer et al. 2005), and such dust is often associated with regular molecular gas kinematics (Alatalo et al. 2013). We therefore began an ALMA campaign to map CO (2−1) kinematics in nearby ETGs with targets selected based on dust morphology. With our ALMA Cycle 2 sample (Boizelle et al. 2017, hereafter Paper I), we demonstrated that the molecular gas disks were both dynamically cold (with the ratio of intrinsic line width to circular speed $\ll 1$) and typically only mildly warped. The disks can be nearly ideal probes of the central gravitational potential and are very amenable to detailed gas-dynamical modeling. Barth et al. (2016b) first demonstrated ALMA's power to constrain BH masses, and follow-up CO imaging at high angular resolution for two targets in our Cycle 2 sample has enabled $M_{\rm BH}$ determinations with percent-level BH mass precision (Barth et al. 2016a; Boizelle et al. 2019, hereafter Paper II). Other groups have simultaneously pioneered this new avenue for measuring BH masses in similar targets (Onishi et al. 2015, 2017; Davis et al. 2017, 2018; Nagai et al. 2019; North et al. 2019; Smith et al. 2019; Vila-Vilaro et al. 2019) with typical ∼10%–20% precision, and the method has been applied to spiral galaxies (Nguyen et al. 2020) and dwarf elliptical galaxies (Davis et al. 2020) as well.

As part of our ALMA program, we selected NGC 315 and NGC 4261 for CO (2−1) observations after identifying 2″- to 3″-wide, morphologically round dust disks in archival HST imaging. Previous CO emission-line surveys reported a tentative CO detection for NGC 315, corresponding to $\log_{10}[M_{\rm H2}/M_\odot] \sim 7.91$, while NGC 4261 was undetected, with an H_2 mass upper limit of $\log_{10}[M_{\rm H2}/M_\odot] \lesssim 7.68$ (Combes et al. 2007; Ocaña Flaquer et al. 2010; Young et al. 2011; Davis et al. 2019). Nevertheless, we expected to easily detect and resolve the disks with ALMA. For comparison, there has been a $\log_{10}[M_{\rm H2}/M_\odot] \lesssim 6.0 - 6.8$ threshold for similar, nearby ($\lesssim$100 Mpc) targets observed with ALMA (Paper I; Ruffa et al. 2019b). We expected both galaxies to fall at the upper end of the BH scaling relations given the stellar velocity dispersions and luminosities reported in the HyperLeda database (Makarov et al. 2014). Based on their large anticipated $r_{\rm g}$, we imaged CO (2−1) in NGC 315 and NGC 4261 at ∼0.″3 resolution in order to at least partially resolve CO kinematics within the BH-dominated regions.

NGC 315 dominates a sparse group environment (Nolthenius 1993; Crook et al. 2007) near the confluence of galaxy filaments in the Pisces-Perseus supercluster (Ensslin et al. 2001). It is a Fanaroff-Riley (FR) type I (Laing et al. 2006) cD galaxy (de Vaucouleurs et al. 1991). At its center resides a type 1.9 low-ionization nuclear emission region (LINER; Ho et al. 1997), with unresolved nonstellar emission detected at radio to X-ray wavelengths (Venturi et al. 1993; Worrall et al. 2007; Gu et al. 2007). Redshift-independent distances for the galaxy from the NASA/IPAC Extragalactic Database[7] range from ∼50 to 100 Mpc, and a forthcoming surface brightness fluctuation (SBF) distance measurement (Goullaud et al. 2018) should clarify the uncertainty. Here we adopt the Hubble flow distance assuming the Virgo + Great Attractor + Shapley Supercluster inflow model for a ΛCDM cosmology with $\Omega_{\rm matter} = 0.308$, $\Omega_{\rm vacuum} = 0.692$, and $H_0 = 67.8$ km s^{-1} Mpc^{-1} (Planck Collaboration et al. 2016). This assumption corresponds to a luminosity distance of 72.3 Mpc, an angular size distance of 70.0 Mpc, and an angular scale of 340 pc arcsec^{-1}. The derived $M_{\rm BH}$ scales linearly with the assumed distance, so any change to the distance will result in a commensurate shift in $M_{\rm BH}$. No previous study has constrained the NGC 315 BH mass.

NGC 4261 (3C 270) is the brightest galaxy in the NGC 4261 group (Davis et al. 1995) in the direction of the Virgo Cluster. This FR I (Jaffe & McNamara 1994) E2-3 galaxy (de Vaucouleurs et al. 1991) has a distance modulus from an SBF measurement of $m - M = 32.50 \pm 0.19$ mag (Tonry et al. 2001), which translates to a luminosity distance of 31.6 ± 2.8 Mpc. Using the observed redshift of $z = 0.00746$ (Huchra et al. 2012), the angular size distance is 31.1 Mpc, and we adopted an angular scale of 150.9 pc arcsec^{-1}. Two previous studies estimated a BH mass of $\sim 5 \times 10^8$ $M_\odot$ for NGC 4261 (Ferrarese et al. 1996; Humphrey et al. 2009).

In this paper, we present the first ALMA 12 m CO imaging of NGC 315 and NGC 4261. While the focus remains on our ∼0.″3 resolution CO (2−1) observations, we also include additional CO (3−2) imaging of NGC 4261 from the ALMA archive to test the robustness of the CO (2−1) gas-dynamical modeling results. The paper is organized as follows. In Section 2, we describe the HST and Spitzer Space Telescope observations used to measure the galaxies' stellar surface brightness distributions. In Section 3, we introduce the ALMA CO imaging. We summarize our gas-dynamical modeling method and results in Section 4 and include an examination of various sources of uncertainty in the $M_{\rm BH}$ determination. In Section 5, we compare to the BH−galaxy scaling relations, discuss future improvements to the ALMA-based $M_{\rm BH}$ measurements, and examine prospects for precision BH mass determination in galaxies with millimeter/submillimeter-bright nuclei. We conclude in Section 6.

2. Optical and Infrared Observations

We used HST Wide Field Camera 3 (WFC3; Dressel 2019) infrared (IR) data to determine luminous mass distributions for NGC 315 and NGC 4261, and WFC3/IR and Wide Field Planetary Camera 2 (WFPC2; Holtzman et al. 1995) optical imaging to quantify the potential impact of dust on our luminous mass models. In order to accurately constrain the stellar halos in these galaxies, we supplemented the HST data with large-scale Spitzer InfraRed Array Camera (IRAC; Fazio et al. 2004) observations. Below we summarize the observations, present surface brightness measurements, and explain dust extinction models.

2.1. HST Imaging

For NGC 315, we retrieved archival WFC3/IR data (GO-14219; Goullaud et al. 2018) taken in the F110W filter (hereafter *J*-band), which covers the inner 2.′1 × 2.′2 region of the galaxy. We combined calibrated *J*-band frames using `AstroDrizzle` (Gonzaga et al. 2012) to produce a final mosaic with a 0.″08 pixel^{-1} scale. We did not remove the background level during the drizzling process. In Figure 1, we

[7] http://ned.ipac.caltech.edu

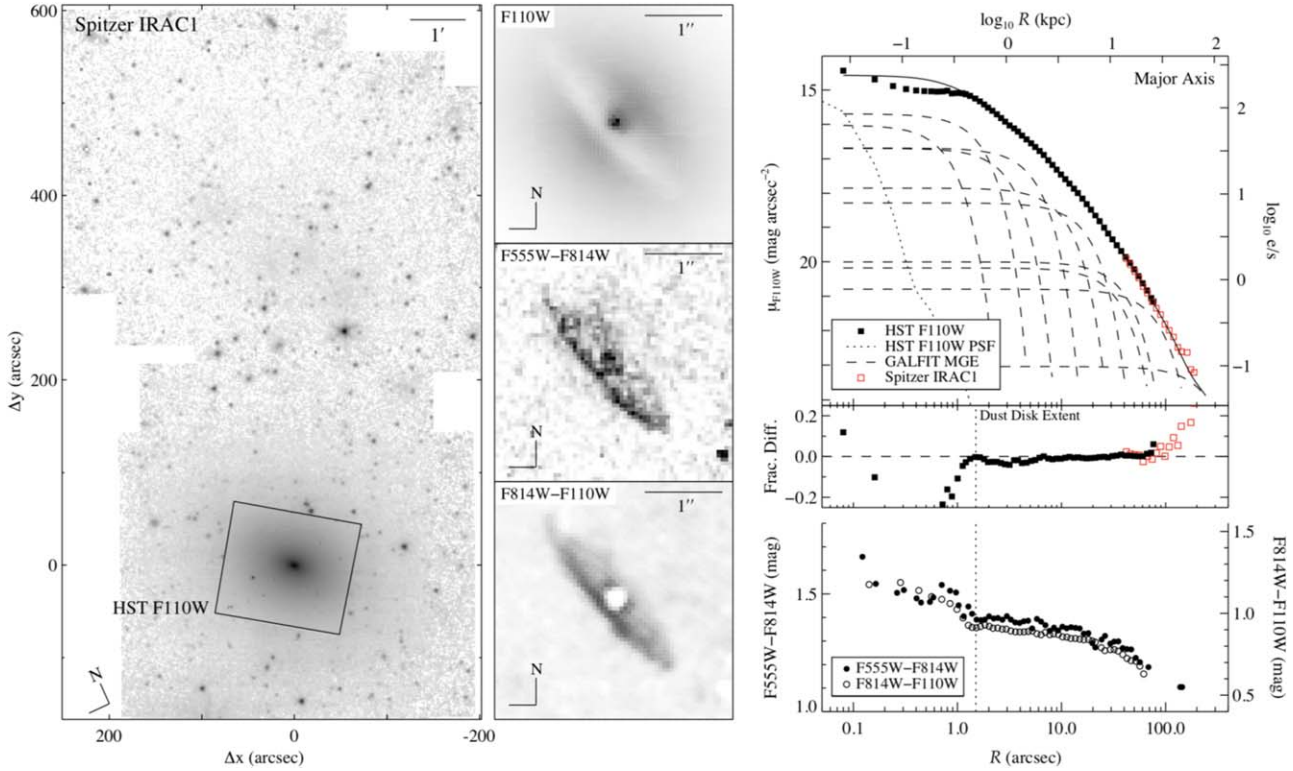

Figure 1. Optical to mid-IR imaging of NGC 315. The HST WFC3 F110W image is overlaid on a Spitzer IRAC1 mosaic (left panel), shown using a logarithmic intensity scale. F555W−F814W and F814W−F110W color maps (shown in central $4\farcs1 \times 4\farcs1$ cutout regions; middle panels) trace a morphologically regular and highly inclined dust disk. Luminous mass models for this galaxy were constructed by parameterizing the *J*-band stellar surface brightness using a GALFIT MGE (top right panel) accompanied by a nuclear point-source component. Here we augmented the HST measurements with larger-scale IRAC1 data. The ($A_J = 0$ mag) MGE solution shown here and in Table 1 was derived after masking the most dust-obscured regions seen in the *J*-band cutout.

show the final *J*-band image that probes the stellar surface brightness out to $R \sim 100''$ (∼34 kpc). The highly inclined dust disk noticeably suppresses stellar light even in the *J*-band image.

For NGC 4261, we obtained new WFC3/IR data (GO-15909; PI: Boizelle) taken in the F160W (hereafter *H*-band) filter and the *J*-band filter. For the *H*-band observations, we used a large-scale mosaic pattern to probe the galaxy light out to $R \sim 150''$ (∼23 kpc) and short subarray exposures taken in a four-point dither pattern centered on the nucleus to sample the point-spread function (PSF) well. In contrast, the *J*-band observations consisted of four-point and two-point dithered subarray exposures covering a $\sim 1\farcs2 \times 1\farcs0$ field. We created composite images with a pixel scale of $0\farcs08$ pixel^{-1} for each filter and sequence using AstroDrizzle. To construct a final *H*-band image, we replaced the central portions of the drizzled large-scale mosaic with the subarray data. Except for a region to the northeast on the dust disk's near side (see Figure 2), the *H*-band data appear largely unaffected by circumnuclear dust.

In order to characterize the dust attenuation properties in the two galaxies (see Section 2.4), we obtained additional optical data from the HST archive. For NGC 315, we retrieved WFPC2 F555W and F814W images (GO-6673; Verdoes Kleijn et al. 1999) and aligned these data to the *J*-band mosaic using TweakReg (Gonzaga et al. 2012). To take advantage of the better angular resolution, we drizzled the WFPC2 data to a $0\farcs05$ pixel^{-1} scale. For NGC 4261, we retrieved WFPC2 data taken in the F547M and F791W filters (GO-5124; Ferrarese et al. 1996), which avoid prominent emission lines from the active galactic nucleus (AGN). These data were likewise drizzled to $0\farcs05$ pixel^{-1} scales before being manually aligned to the *H*-band mosaic. As demonstrated in Figures 1 and 2, the observed optical color gradients for NGC 315 and NGC 4261 are consistent with those measured for other massive, red ETGs (e.g., La Barbera et al. 2010; Kennedy et al. 2016).

2.2. Spitzer Imaging

For both NGC 315 and NGC 4261, we retrieved IRAC channel 1 (3.6 μm) data from the Spitzer Enhanced Imaging Products archive.[8] In addition to sensitivity considerations, we selected this channel to trace the old stellar population while avoiding emission-line contamination in redder filters. The IRAC1 supermosaics shown in Figures 1 and 2 cover both galaxies out to $R \sim 11'$ (∼225 and 100 kpc for NGC 315 and NGC 4261, respectively). We measured and removed any residual background from the Spitzer data using uncontaminated regions far from the primary targets.

2.3. Stellar Luminosity Profile

The NGC 315 and NGC 4261 stellar halos clearly extend beyond the HST IR mosaics. Following the method outlined in Paper II, we used large-scale Spitzer imaging to constrain IR zodiacal background levels (Pirzkal 2014) and to extend stellar surface brightness measurements. After masking galaxies and foreground stars, we measured WFC3/IR and IRAC1 surface brightness profiles for NGC 315 and NGC 4261 in directions

[8] http://irsa.ipac.caltech.edu/data/SPITZER/Enhanced/SEIP/overview.html

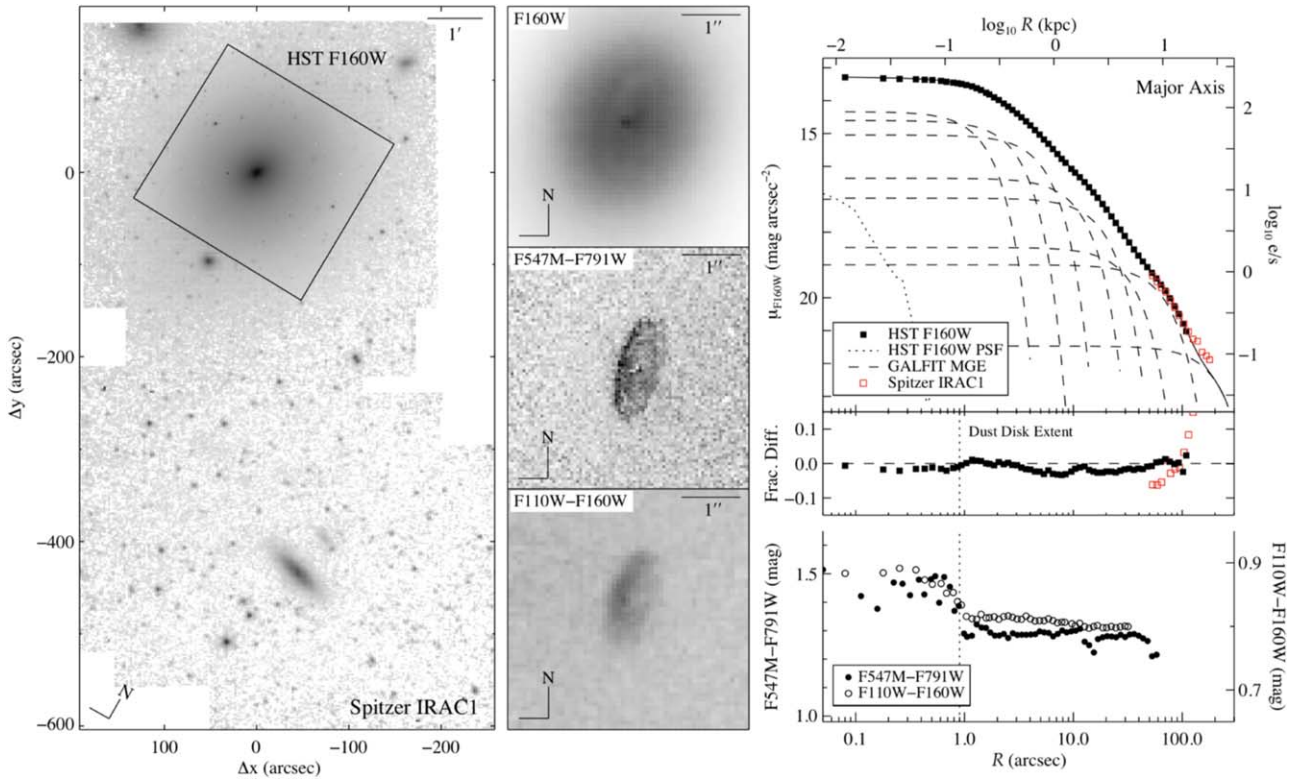

Figure 2. Optical to mid-IR imaging of NGC 4261. The HST WFC3 F160W image is overlaid on a Spitzer IRAC1 mosaic (left panel), shown using a logarithmic intensity scale. The F547M−F791W and F110W−F160W color maps (shown in central $4\farcs1 \times 4\farcs1$ cutout regions; middle panels) reveal a round circumnuclear dust disk that is slightly miscentered relative to the stellar bulge. The luminous mass model for this galaxy was constructed by parameterizing the *H*-band surface brightness using a GALFIT MGE and a central point-source component (top right panel). These HST measurements were augmented with larger-scale IRAC1 data. The ($A_H = 0$ mag) MGE solution shown here and in Table 1 was derived after masking the reddest IR colors in the *H*-band cutout, which are expected to trace the most dust-obscured regions.

toward the outermost edges of the 3.6 μm supermosaics. Using overlapping measurements between $R \sim 50''$ and $100''$, we simultaneously determined a background level of $\mu_J = 21.68$ mag arcsec^{-2} and a color of $J - \mathrm{IRAC1} = 1.53$ mag needed to align the NGC 315 measurements. Likewise, we determined a background level of $\mu_H = 20.44$ mag arcsec^{-2} with $H - \mathrm{IRAC1} = 0.72$ mag for NGC 4261. Nearly identical values were obtained when matching HST and Spitzer surface brightness profiles along different directions.

To characterize the stellar luminosity distributions, we modeled both the WFC3/IR mosaics and flux-scaled IRAC1 images with concentric 2D Gaussian functions using GALFIT (Peng et al. 2002). Preliminary parameter guesses were obtained using the Cappellari (2002) Multi-Gaussian Expansion (MGE) code, and the major-axis position angles (PAs) of the Gaussian components were tied together. We adopted Tiny Tim models (Krist & Hook 2004) that were dithered and drizzled identically to the HST observations to account for PSF blurring when modeling the WFC3/IR data. For the IRAC1 observations, we employed an empirical model of the Spitzer point response function (Hoffmann et al. 2004).

We started by fitting MGEs to the WFC3 and IRAC1 images separately. The largest Spitzer MGE FWHMs were at least twice that of the outermost HST MGE component, so we incorporated the outermost IRAC1 Gaussians into the initial HST MGE. We then reoptimized the MGE fits to the WFC3 mosaics only, holding fixed the (scaled) magnitudes and FWHMs of the extended IRAC1 Gaussian components while tying their centroids and PAs to those of the inner HST Gaussian components. Such large-scale information is not necessary for the gas-dynamical models described here, but these MGEs may be useful for future studies of the galaxies (e.g., stellar-dynamical modeling).

2.3.1. Application to NGC 315

Circumnuclear dust significantly obscures the central stellar light of NGC 315, even at the WFC3/IR wavelengths. The impact of dust is explored more in Section 2.4, but we constructed the first of our *J*-band MGEs after simply masking the most dust-obscured pixels where $I - J > 0.96$ mag. The mask excludes filamentary dust features to the south and west of the nucleus and the entire disk region except for the central few pixels and those behind (to the northwest of) the galaxy center. Initial GALFIT fits preferred the innermost Gaussian to be very compact (FWHM $<0\farcs01$), consistent with unresolved emission from the AGN. To account for nonstellar contributions in the GALFIT fit, we included a concentric PSF component that follows the F110W Tiny Tim model.

By comparing the data and MGE model, we estimate that the intrinsic disk extinction may reach as high as $A_J \sim 1.4$ mag at a semimajor-axis distance of $R \sim 0\farcs5$. This MGE solution (shown in Figure 1 and in Table 1) consists of 10 Gaussian components, with the outermost two Gaussians based on the large-scale Spitzer surface brightness. Each of the Gaussian magnitudes was corrected for Galactic reddening, assuming $A_{J,\mathrm{Gal}} = 0.057$ mag toward NGC 315 (Schlafly & Finkbeiner 2011). The model's *J*-band luminosity measured within the central $300''$ ($\sim$100 kpc) is $L_J = 5.79 \times 10^{11}\ L_\odot$, and we estimate a circularized half-light radius (Cappellari et al. 2013)

Table 1
MGE Parameters

j (1)	$\log_{10} I_{J,j}$ ($L_\odot$ pc^{-2}) (2)	σ'_j (arcsec) (3)	q'_j (4)	$\log_{10} I_{H,j}$ ($L_\odot$ pc^{-2}) (2)	σ'_j (arcsec) (3)	q'_j (4)
	NGC 315			NGC 4261		
1	3.798	0.580	0.871	4.261	1.075	0.830
2	3.895	1.237	0.786	4.143	2.131	0.717
3	3.485	2.347	0.704	3.964	3.837	0.729
4	3.483	4.132	0.722	3.437	8.191	0.719
5	3.017	8.191	0.664	3.194	13.54	0.834
6	2.844	13.25	0.748	2.595	23.79	0.816
7	2.085	26.51	0.763	2.381	49.05	0.862
8	2.155	30.90	0.689	1.392*	144.4*	0.820*
9	1.839*	61.95*	0.810*	…	…	…
10	0.939*	192.6*	0.980*	…	…	…

Note. NGC 315 and NGC 4261 MGE solutions constructed from their respective J- and H-band mosaics. For NGC 315, the MGE has a uniform PA = 44.°31 for all components, while PA = − 22.°03 for the best-fit NGC 4261 model. Column (1) lists the component number, Column (2) is the central surface brightness assuming absolute solar magnitudes of $M_{\odot,J} = 3.82$ mag and $M_{\odot,H} = 3.37$ mag (Willmer 2018), Column (3) gives the Gaussian standard deviation along the major axis, and Column (4) provides the component axis ratio. Primes indicate projected quantities. Spitzer IRAC1 MGE components identified with an asterisk were scaled to match the WFC3/IR data and included as fixed components when fitting MGEs to the HST images. The unresolved nuclear features were modeled as point sources during the MGE fit with GALFIT and have apparent magnitudes of $m_J \approx 19.2$ mag and $m_H \approx 19.6$ mag for NGC 315 and NGC 4261, respectively.

of $R_e = 56.''0$ (∼19.0 kpc) in this filter, roughly a factor of two larger than curve-of-growth estimates (van den Bosch 2016; Veale et al. 2017).

2.3.2. Application to NGC 4261

While much less apparent than for NGC 315, circumnuclear dust still reduces the central surface brightness of the NGC 4261 WFC3/IR data. We started by masking the most likely dust-obscured regions, excluding pixels where $J - H > 0.85$ mag to the south of the nucleus and along the disk's eastern (near) side. We then parameterized the H-band data with a GALFIT MGE and a PSF component. In the same manner as done for NGC 315, we included the single most extended Spitzer MGE component as a fixed Gaussian during the fit to the HST data. This MGE solution, shown in Figure 2 and in Table 1, has eight Gaussian components, each of which was corrected for Galactic reddening assuming $A_{H,\mathrm{Gal}} = 0.009$ mag toward NGC 4261 (Schlafly & Finkbeiner 2011). The model's total H-band luminosity measured within the central 300″ (∼45 kpc) is $L_H = 2.29 \times 10^{11}\ L_\odot$, and we found $R_e = 36.''2$ (∼5.5 kpc), which is in good agreement with an average of early curve-of-growth estimates (Cappellari et al. 2011) but is roughly 30% smaller than more recent values (Cappellari et al. 2013; van den Bosch 2016).

2.4. Disk Extinction Modeling

Based on our previous analysis in Paper II, even a modest change in the central stellar contribution to the gravitational potential can produce a shift in the best-fit M_{BH} that far exceeds both the statistical uncertainty from dynamical modeling and most other systematic error terms. Therefore, using HST color maps, we determined a plausible range of central extinction values, following the method outlined here and described in greater detail in Paper II (see also Goudfrooij et al. 1994; Viaene et al. 2017).

Our method assumes that a geometrically thin, inclined dust disk lies in the midplane of an oblate axisymmetric galaxy. If the dust disk has a very low optical depth, then we expect there to be little to no color excess. The same is true if the disk has a very high optical depth because the starlight behind the disk is completely obscured. For some moderate value of disk optical depth, the color excess should be large, as some starlight passes through the disk but becomes reddened. Therefore, the color excess should increase, reach a maximum value, and then decrease as the disk optical depth increases. In addition, we expect there to be a spatial dependence due to the inclined nature of the disk. For a particular value of the disk optical depth, the near side of the disk should have a larger color excess compared to the far side of the disk because there is a larger fraction of starlight behind the near side of the disk. We indeed see such behavior when employing a simple embedded screen model, as discussed below.

After deprojecting the NGC 315 MGE in Table 1 for an inclination angle $i = 75°$ (inferred from our initial gas-dynamical models), we estimated the fraction of total stellar light originating from behind the midplane on a pixel-by-pixel basis. Adopting a ratio of total to selective extinction of $R_V = 3.1$ (Mathis 1990), we determined model color excess curves as a function of the intrinsic extinction A_V of the obscuring disk. Comparing the model color excess curves with the data (Figure 3) suggests extinction values of $A_V \sim 3-4$ mag ($A_J \sim 1-1.5$ mag) at a projected $R \sim 0.''2$ from the nucleus along the minor axis.

In addition to the initial ($A_J = 0$ mag) MGE solution presented in Figure 1 and Table 1, we constructed two other luminous mass models for NGC 315 to cover the plausible range in A_J. To start, we masked nearly the entire dust disk as described in Section 2.3.1 before fitting the J-band mosaic for $R < 10''$ using a PSF-convolved Nuker function (Lauer et al. 1995) and a concentric PSF component in GALFIT. The best-fit model has inner and outer power-law slopes of $\gamma = 0.0$ and $\beta = 1.48$, respectively, with a break radius $r_b = 1.''42$ and a transition sharpness $\alpha = 1.54$. After subtracting the point-source component, we corrected the central unmasked surface brightness values for extinction levels of $A_J = 0.75$ and 1.50 mag. Next, we refit surface brightnesses corrected for each A_J value in turn with a Nuker function while fixing $\beta = 1.48$ and $r_b = 1.''42$. For the $A_J = 0.75$ and 1.50 mag cases, we found $\gamma = 0.18$ and 0.33, respectively. The best-fit γ for the $A_J = 1.50$ mag case is at the boundary between those of core and power-

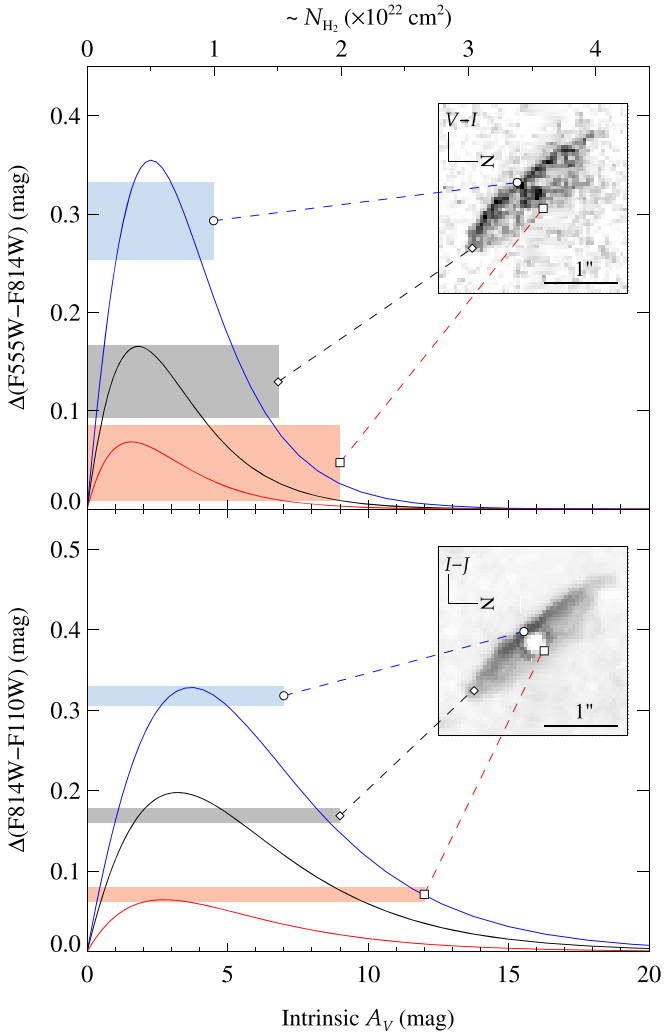

Figure 3. Comparison between observed color excesses at the marked locations on the NGC 315 HST F555W−F814W and F814W−F110W maps and the curves expected for a simple dust attenuation model. Shaded rectangles encompass the range of observed color values about the marked spatial locations. Agreement between observations and the model along the ring of maximal observed color suggests that the stellar light behind the galaxy's midplane is obscured by dust reaching an intrinsic $A_V \sim 3-4$ mag ($A_J \sim 1-1.5$ mag) at a projected separation of $R \sim 0\farcs2$ from the nucleus along the minor axis. H_2 column densities were estimated using a Galactic N_{H_2}/A_V ratio (Güver & Özel 2009).

law galaxies (e.g., Faber et al. 1997). To construct "dust-corrected" luminous mass models, we replaced the *J*-band data within the disk region with the best-fit Nuker models. We optimized MGE models with `GALFIT` to the "corrected" images in nearly the same manner as before, although we did not apply a dust mask. The "dust-corrected" MGEs are given in Table A1 in the Appendix, and Figure 4 compares the data and the three model surface brightness profiles.

The NGC 4261 *H*-band mosaic is not as visibly affected by dust as are the NGC 315 WFC3/IR data. To estimate the magnitude of the obscuration, we applied the same dust modeling technique used for NGC 315. Adopting $i = 64°$ from fits to the dust disk morphology (Ferrarese et al. 1996), we deprojected the NGC 4261 initial ($A_H = 0$ mag) MGE presented in Figure 2 and Table 1 and compared the model and observed $J - H$ color excesses. The maximal observed color excesses are consistent with $A_H \lesssim 0.4$ mag at all radii. We then constructed a "dust-corrected" MGE, first masking regions of the dust disk with high color excess ($\Delta(J-H) > 0.05$) before fitting the *H*-band mosaic within $R < 10''$ using a PSF-convolved Nuker function and a concentric PSF component. The best-fit Nuker model has power-law slopes of $\gamma = 0.03$ and $\beta = 1.43$, with $r_b = 1\farcs72$ and $\alpha = 2.47$. After subtracting the point-source component, we corrected the central surface brightness values for $A_H = 0.4$ mag and fit the corresponding surface brightnesses using a Nuker function with fixed $\beta = 1.43$ and $r_b = 1\farcs72$, finding a best-fit inner slope of $\gamma = 0.10$. We replaced the *H*-band surface brightness values within the dust disk region with the Nuker model and constructed an MGE that fit the "corrected" image without including a dust mask. We compare the data and model surface brightness profiles in Figure 4 and present the "dust-corrected" MGE in Table A1 in the Appendix.

3. ALMA Data

3.1. Observations and Data Processing

We obtained ALMA imaging of NGC 315 and NGC 4261 in the C43−5 configuration in Program 2017.1.00301.S. Observations consisted of a single pointing with four ∼2 GHz bandwidth spectral windows: one was centered on the redshifted CO (2−1) 230.538 GHz line, two others measured the continuum at average sky frequencies of 228.4 and 243.0 GHz, and one was designed for the possible detection of redshifted CS (5−4) 244.935 GHz line emission. For NGC 315, data were obtained during Cycle 6 in three execution blocks spanning 2018 October 19–November 19. Excluding data with a quality assurance rating of "semi-pass," the total on-source integration time was 89 minutes. For NGC 4261, our data were obtained during Cycle 5 with a single execution block on 2018 January 19 and had an on-source integration time of 31.5 minutes. The data were flux-calibrated using ALMA quasar standards J2253+1608 and J1229+0203, which have absolute flux calibration uncertainties of ∼10% at 1 mm (Fomalont et al. 2014). We have propagated this systematic uncertainty into all subsequent flux and flux density measurements and quantities derived from them.

Visibilities were calibrated using version 5.1.2 of the `Common Astronomy Software Applications` (`CASA`; McMullin et al. 2007) package. We used the bright ($S_{230\,\mathrm{GHz}} = 0.2-0.25$ Jy) continuum emission at the centers of NGC 315 and NGC 4261 to apply phase and amplitude self-calibration. Following *uv*-plane continuum subtraction, the CO (2−1) spectral window data were deconvolved using `CASA tclean` with Briggs (Briggs 1995) weighting of $r = 0.5$. While we detect resolved 1.3 mm continuum in both galaxies and centrally concentrated CS (5−4) emission in NGC 315, we focus here only on the CO emission. For NGC 315, the synthesized beam at a sky frequency of ∼229 GHz has $\theta_{\mathrm{FWHM}} = 0\farcs35 \times 0\farcs22$ oriented at PA = 15°.7. We imaged the primary spectral window into a CO (2−1) cube with $0\farcs035$ pixels and 7.81 MHz channels, corresponding to rest-frame velocity widths of about 10.3 km s^{-1} and resulting in typical rms sensitivities of ∼0.35 mJy beam^{-1}. At the same frequency for NGC 4261, imaging yields $\theta_{\mathrm{FWHM}} = 0\farcs31 \times 0\farcs28$ at PA = 51°.9. Due to low signal-to-noise ratio (S/N) of the CO (2−1) line, we imaged NGC 4261 using coarser channels of 31.2 MHz (rest-frame 40.9 km s^{-1}), with an rms sensitivity of ∼0.26 mJy beam^{-1} per channel. For the NGC 4261 CO (2−1) cube, we also selected a larger pixel size of $0\farcs05$ pixel^{-1} to appropriately sample θ_{FWHM}.

Just 2 days after our data were taken, ALMA observed NGC 4261 in Band 7 as a part of Program 2017.1.01638.S (PI: Kameno). One of the spectral windows had usable data extending

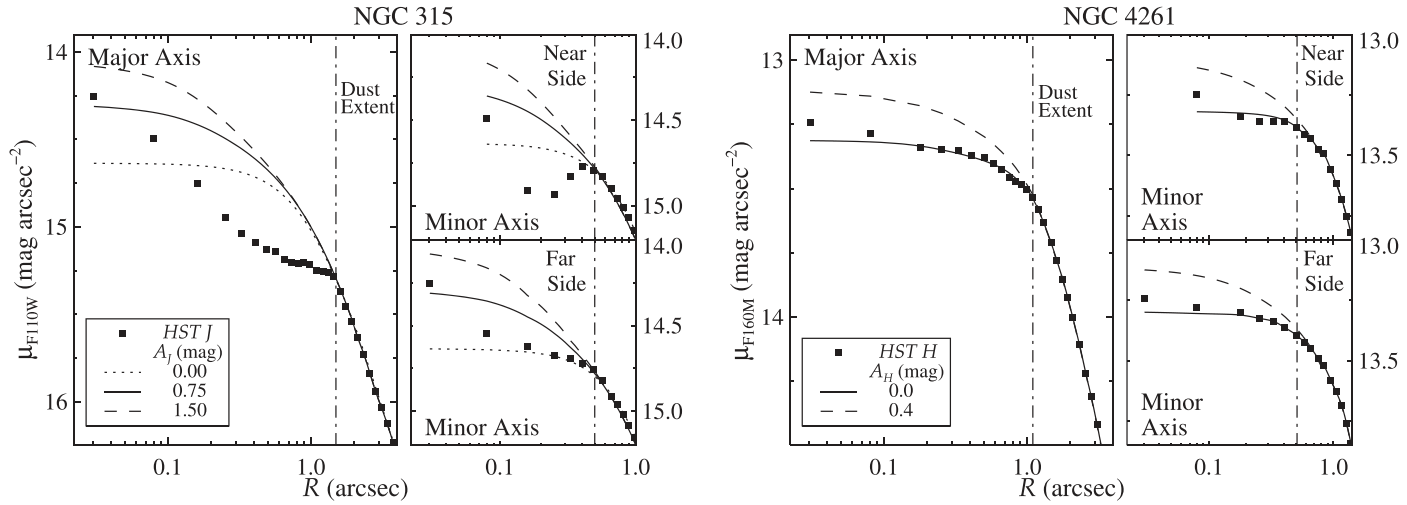

Figure 4. Comparison between the observed NGC 315 *J*-band and NGC 4261 *H*-band surface brightness profiles and those derived from extinction-corrected MGE models. For NGC 315, we show both the dust-masked ($A_J = 0$ mag) model and MGEs constructed after correcting central surface brightness values for $A_J = 0.75$ and 1.50 mag of extinction of the light behind the disk. For NGC 4261, we show the dust-masked ($A_H = 0$ mag) model along with an MGE solution corrected for a central extinction of $A_H = 0.4$ mag. The minor-axis plots (right panels) show NGC 315 and NGC 4261 surface brightness profiles taken along the near (southeast and east of the nuclei, respectively) and far sides of the dust disks. We note that the central *J*- and *H*-band excesses are fit as point sources with no extinction correction and are not included in the MGE models.

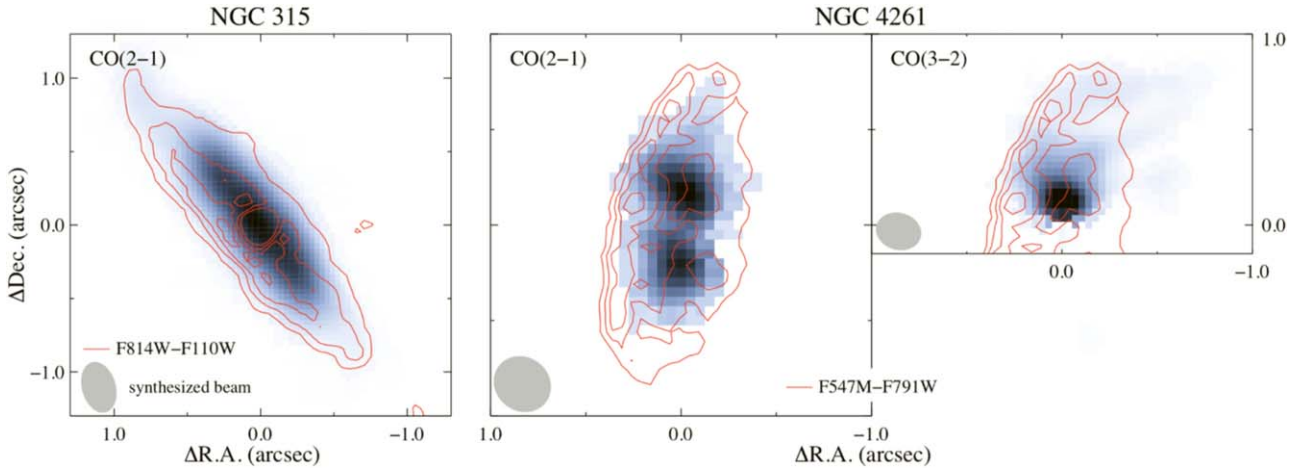

Figure 5. CO (2−1) and CO (3−2) zeroth-moment maps measured from the NGC 315 and NGC 4261 ALMA data sets. The frequency range of the archival NGC 4261 CO (3−2) observations excludes most of the emission on the approaching (south) side of the disk. Contours show the respective HST $I - J$ and $V - I$ colors. The CO emission in each galaxy is concentrated within the region enclosed by the maximum HST color contours.

from 341.75 to 343.45 GHz, which covers the CO (3−2) line on the receding side of the disk, down to line-of-sight velocities (v_{LOS}) of −158 km s^{-1} relative to the galaxy's systemic velocity (v_{sys}). We retrieved the Band 7 data to complement our CO (2−1) observations and reduced them using the same approaches to self-calibration and *uv*-plane continuum subtraction. We then imaged the visibilities into a CO (3−2) data cube with 0.″035 pixels and 15.6 MHz (rest-frame 13.8 km s^{-1}) channels with ∼0.34 mJy beam^{-1} point-source sensitivities. At a sky frequency of ∼344 GHz, the Band 7 data have $\theta_{FWHM} = 0.''24 \times 0.''19$ at PA = 75.°2, resulting in 30% better average linear resolution than our CO (2−1) observations.

3.2. Emission-line Properties

The CO emission in the ALMA spectral cubes traces molecular gas in regular rotation about their respective galaxy centers. This CO emission originates from the same region as the arcsecond-scale dust disks detected in the HST color maps, as shown in Figure 5. We constructed maps of the first three line moments, all of which are presented in Figure 6, after applying masks to exclude pixels that did not contain line emission. To ensure smooth first- and second-moment maps, especially in the outer-disk regions, spectra were co-added in spatial bins to achieve higher S/N using a Voronoi tessellation technique (Cappellari & Copin 2003).

We created CO position–velocity diagrams (PVDs) by extracting data from the NGC 315 cube along PA = 39° and from the NGC 4261 cubes along PA = −5° using spatial extraction widths equal to the averages of their synthesized beam FWHMs. The CO emission reveals quasi-Keplerian rotation due to a central BH and an extended mass distribution. The gas velocities rise at projected distances of ∼15−30 pc from the galaxy centers, where the BHs dominate the gravitational potentials. The innermost CO (2−1) emission in NGC 315 has a maximum $v_{LOS} \sim 500$ km s^{-1} relative to v_{sys}, corresponding to $M_{BH} \sim 2.1 \times 10^9\ M_\odot$ after assuming a disk

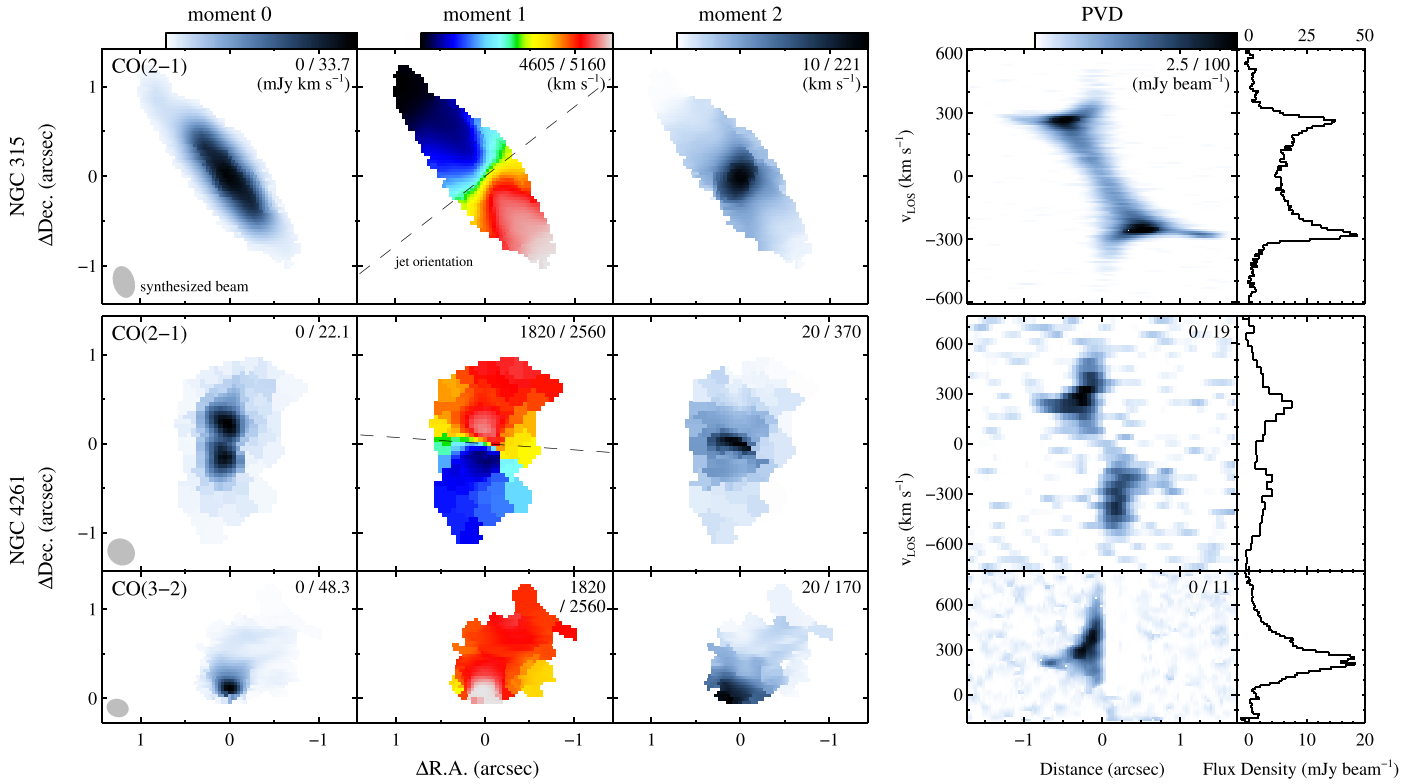

Figure 6. Moment maps constructed from NGC 315 CO (2−1) (top panels) and NGC 4261 CO (2−1) and CO (3−2) (middle and bottom panels) ALMA data cubes. The moment maps reveal regular, albeit slightly warped, disk rotation. In the outer-disk regions, spectra were binned together to achieve higher S/N. The moment values are linearly mapped to colors, shown by the color bar at the top of the maps, and the ranges in each panel indicate the minimum and maximum values of each color bar. The orientation of the radio jets (dashed lines) is roughly perpendicular to the lines of nodes. Major-axis PVDs (right panels) are displayed with their $v_{\rm LOS}$ relative to $v_{\rm sys}$ from Table 3, with color bar ranges in each panel. Velocity profiles (far right panels) for each cube were constructed by integrating flux densities within mask regions that follow the emission observed in each channel.

$i \approx 75°$. For NGC 4261, the innermost CO (2−1) and CO (3−2) emission reaches $|v_{\rm LOS} - v_{\rm sys}| \sim 590$ and 660 km s^{-1}, respectively, suggesting $M_{\rm BH} \sim (1.5{-}1.6) \times 10^9\ M_\odot$ for $i \approx 65°$. The loci of high-velocity CO emission in the NGC 315 and NGC 4261 data sets remain more blended with minor-axis emission (with $v_{\rm LOS} \sim v_{\rm sys}$) than the spectacularly well-resolved cases of NGC 3258 (Paper II) and NGC 383 (North et al. 2019). The greater degree of blending is driven by both higher disk inclination angles and the factor of ∼3 larger $\theta_{\rm FWHM}$ of our Cycle 5 and 6 observations compared to those papers' data.

All three zeroth-moment maps in Figure 6 show apparently smooth, centrally concentrated CO emission, although the corresponding physical resolutions of 30−100 pc preclude any conclusions about CO substructure on cloud scales of a few to ∼30 pc (e.g., Utomo et al. 2015; Faesi et al. 2018). We measured a total CO (2−1) flux of $12.37 \pm 0.06({\rm stat}) \pm 1.24({\rm sys})$ Jy km s^{-1} for NGC 315 (quoting statistical and systemic uncertainties, respectively) and $3.06 \pm 0.15({\rm stat}) \pm 0.31({\rm sys})$ Jy km s^{-1} for NGC 4261. Due to the incomplete Band 7 spectral coverage, we cannot confidently estimate the total CO (3−2) flux of the NGC 4261 disk. After degrading the CO (3−2) cube angular resolution to match that of the NGC 4261 CO (2−1) data, we determined the CO line luminosities in temperatures units ($L'_{\rm CO}$; Carilli & Walter 2013) over the data sets' common velocity range and measured a ratio $R_{32} = L'_{\rm CO32}/L'_{\rm CO21}$ of ∼0.3−0.4 in the outer disk that rises to ∼0.6 near the nucleus. This rise in R_{32} hints at a modest central increase in gas temperature and/or density.

We estimated H_2 gas masses assuming a line luminosity ratio $R_{21} = L'_{\rm CO21}/L'_{\rm CO10} = 0.7$ and adopting a CO (1−0)-to-H_2 conversion factor $\alpha_{\rm CO} = 3.1\ M_\odot$ pc^{-2} (K km s^{-1})$^{-1}$ from a sample of nearby, late-type galaxies (Sandstrom et al. 2013). We then computed total gas masses ($M_{\rm gas}$) by correcting the H_2 mass measurements for the helium mass fraction $f_{\rm He} = 0.36$. For NGC 315, the implied disk mass of $(M_{\rm gas}/10^8\ M_\odot) = 2.39 \pm 0.01$ (stat) $\pm$ 0.24(sys) is consistent with previous upper limits (Davis et al. 2019) and a tentative detection based on single-dish observations ($\log_{10}[M_{\rm gas}/M_\odot] \sim 7.9$ after correcting for our assumed distance, $\alpha_{\rm CO}$, and $f_{\rm He}$; Ocaña Flaquer et al. 2010). In the same manner for NGC 4261, we estimated a total gas mass of $(M_{\rm gas}/10^7\ M_\odot) = 1.12 \pm 0.05({\rm stat}) \pm 0.11({\rm sys})$ that is well below the detection threshold of previous surveys ($\log_{10}[M_{\rm gas}/M_\odot] \sim 7.5 - 7.8$ after correcting for our assumed $\alpha_{\rm CO}$ and $f_{\rm He}$; Combes et al. 2007; Ocaña Flaquer et al. 2010; Young et al. 2011) and is therefore consistent with earlier nondetections. The peak gas mass surface densities ($\Sigma_{\rm gas}$) for the disks in NGC 315 and NGC 4261 are $3.1 \times 10^3\ M_\odot$ pc^{-2} and $1.5 \times 10^3\ M_\odot$ pc^{-2}, respectively, after deprojection. The $M_{\rm gas}$ and peak $\Sigma_{\rm gas}$ values are similar to those from other ETGs hosting few $\times\ 10^2$ pc wide dust disks observed at similar physical resolutions (Paper I; Ruffa et al. 2019b).

To quantify potential deviations from purely circular, thin-disk rotation, we applied the `kinemetry` framework (Krajnović et al. 2011) to the CO first-moment maps and traced the PA of the line of nodes ($\Gamma_{\rm LON}$) as a function of radius. From the NGC 315 disk edge to the center, the gas kinematic PA increases by only $\Delta\Gamma_{\rm LON} \sim 7°$, consistent with measurements from other settled gas disks (Paper I;

Table 2
Dynamical Model Properties

NGC 315					NGC 4261					
Model	Mass Model	A_J (mag)	Disk Inclination (deg)	$\sigma_{\rm turb}(r)$	Model	CO Transition	Mass Model	A_H (mag)	Disk Inclination (deg)	$\sigma_{\rm turb}(r)$
A	MGE; free Υ_J	0	Free i	Uniform	C1	2−1	MGE; free Υ_H	0	Free i	Uniform
B1	MGE; free Υ_J	0	Free i	Gaussian	C2	2−1	MGE; free Υ_H	0.4	Free i	Uniform
B2	MGE; free Υ_J	0.75	Free i	Gaussian	D	2−1	MGE; free Υ_H	0	$i = 60.8$	Exponential
B3	MGE; free Υ_J	1.50	Free i	Gaussian	E	3−2	MGE; free Υ_H	0	$i = 60.8$	Uniform

Note. Properties of the NGC 315 CO (2−1) and NGC 4261 CO (2−1) and CO (3−2) gas-dynamical models, all of which treat the CO emission as arising from a thin, flat disk. Each galaxy's extended mass distribution was determined by deprojecting a *J*- or *H*-band MGE model from either Table 1 or Table A1. The listed A_J or A_H refers to the assumed extinction correction to the portion of the stellar surface brightness originating behind the inclined dust disk. For NGC 4261, we examined two models with a molecular gas disk inclination angle fixed to the best-fit model C value to avoid implausibly low *i*: model D is identical to model C1 except for the different form used for $\sigma_{\rm turb}$, and model E is identical to model C1 except for its application to the CO (3−2) data cube. While optimizing model E, we fixed $v_{\rm sys} = 2207.0$ km s^{-1}, as the CO (3−2) data cube covers only the receding side of the disk.

Smith et al. 2019). We also calculated a global average $\overline{\Gamma}_{\rm LON}$ of 223° (for the receding side), which agrees with both the photometric and stellar kinematic PAs (Ene et al. 2020) while being nearly perpendicular to the radio jet (Ensslin et al. 2001; Lister et al. 2018). From the NGC 4261 CO (2−1) first-moment map, we estimated $\Gamma_{\rm LON} \sim -23°$ at the disk edge, which is consistent with the photometric PA (see also Krajnović et al. 2011) but is misaligned with the stellar kinematic PA (e.g., Davies & Birkinshaw 1986; Krajnović et al. 2011). Near the disk center, $\Gamma_{\rm LON} \sim -10°$ and is roughly perpendicular to the radio jet (Jones & Wehrle 1997). Since $\Delta\Gamma_{\rm LON} > 10°$ over the CO disk and there is an offset in the centroids of the dust disk and stellar bulge (Figure 2; also noted by Jaffe et al. 1996; Ferrarese et al. 1996), the NGC 4261 disk may not yet be fully settled into an equilibrium configuration.

4. Dynamical Modeling

We determined BH masses from the ALMA data following a flat-disk forward-modeling procedure that is briefly summarized here. We refer the reader to the discussion by Barth et al. (2016a, 2016b) and Paper II for more details. After fitting models A−E (outlined in Table 2) to the corresponding CO data cubes, we explored sources of systematic uncertainty in the models to determine final error budgets for the NGC 315 and NGC 4261 BH masses.

4.1. Method

We used models of the CO gas rotation and intrinsic turbulent velocity dispersion ($\sigma_{\rm turb}$) to populate a model cube at each spatial location with Gaussian emergent line profiles. The models were fit directly to the ALMA CO data cubes, thereby allowing better characterization of model goodness of fit than if the fits were made to only moment maps. Model parameters were optimized by χ^2 minimization using a downhill simplex approach (Press et al. 1992).

We began by calculating the circular velocity in the galaxy midplane as a function of radius. The circular velocity ($v_{\rm c}$) arises from the combined gravitational potential of both an extended stellar mass distribution and a BH. We determined the stellar contribution to $v_{\rm c}$ by deprojecting the 2D light distribution parameterized by an MGE and scaling by the mass-to-light ratio Υ. Given the typically small contribution of the molecular gas to the central gravitational potential in ETGs (e.g., Barth et al. 2016b; Davis et al. 2017, 2018; Smith et al. 2019), we did not include the mass of the gas disk in the primary models A−E. However, we did explore the impact on the NGC 315 BH mass of including $M_{\rm gas}$ in the calculation of the total gravitational potential.

By projecting $v_{\rm c}$ for a given i and Γ, with Γ defined as the angle east of north to the receding side of the disk, we determined $v_{\rm LOS}$. Modeling the data cubes also requires assumptions about the intrinsic line widths. Previous ionized gas-dynamical models often required a central rise in the intrinsic line widths (of $\gtrsim$100 km s^{-1}; Verdoes Kleijn et al. 2000; Barth et al. 2001; Walsh et al. 2010) to better match the observed kinematics. Thus, in addition to a spatially uniform $\sigma_{\rm turb} = \sigma_1$, we explored two functional forms for the intrinsic gas velocity dispersion as a function of physical radius r: an exponential profile with $\sigma_{\rm turb}(r) = \sigma_0 \exp[-r/\mu] + \sigma_1$, and a Gaussian profile with $\sigma_{\rm turb}(r) = \sigma_0 \exp[-(r - r_0)^2/2\mu^2] + \sigma_1$. The observed line widths are also the product of rotational broadening that arises from intrapixel velocity gradients. To account for this effect, we oversampled the data cube pixel scale by a factor s such that each pixel is divided into an $s \times s$ grid of elements. Both the model $v_{\rm LOS}$ and $\sigma_{\rm turb}$ maps were calculated on this oversampled grid.

The line profiles were weighted by an approximation for the intrinsic CO surface brightness, formed using the IRAF STSDAS Richardson–Lucy deconvolution task `lucy` (Richardson 1972; Lucy 1974). We input the Voronoi-binned zeroth-moment map and applied 10 iterations of deconvolution, using the ALMA synthesized beam as the kernel. Since the CO surface brightness is not known on subpixel scales, we assumed that each oversampled line profile has the same integrated flux and that the combined $s \times s$ total is equal to the deconvolved value at the native pixel scale. When optimizing the gas-dynamical model, we scaled this approximate flux map by a factor f_0 to account for possible normalization mismatches between the data and model.

The models outlined in Table 2 have between 7 and 12 free parameters each, including $M_{\rm BH}$, a stellar mass-to-light ratio that is either Υ_J or Υ_H, disk i and Γ angles, $\sigma_{\rm turb}(r)$, the kinematic center $(x_{\rm c},y_{\rm c})$, a recessional velocity $v_{\rm sys}$, and the scaling factor f_0. Before comparing the data and model cubes, we downsampled each $s \times s$ grid to the native pixel binning and convolved model cube channels with the ALMA synthesized beam. Since the noise in adjacent spatial pixels remains correlated, we elected to compute the model goodness of fit after spatially block-averaging the data and model in

Table 3
Dynamical Modeling Results for NGC 315 and NGC 4261

Model	$M_{\rm BH}$ ($10^9\ M_\odot$)	Υ ($M_\odot/L_\odot$)	i (deg)	Γ (deg)	σ_1 (km s^{-1})	σ_0 (km s^{-1})	r_0 (pc)	μ (pc)	x_c (arcsec)	y_c (arcsec)	$v_{\rm sys}$ (km s^{-1})	f_0	χ^2_ν
						NGC 315							
A	2.39	2.06	74.1	218.1	15.3	⋯	⋯	⋯	−0.007	0.006	4969.0	0.970	2.046
B1	2.40	2.05	74.1	218.1	15.2	147.3	4.39	32.0	−0.007	0.005	4969.0	0.970	2.036
B2	2.08	1.87	74.2	218.3	15.3	119.9	8.47	21.3	−0.007	0.005	4969.1	0.958	1.992
	(0.01)	(0.01)	(0.1)	(0.1)	$(^{+0.3}_{-0.2})$	$(^{+9.4}_{-3.3})$	$(^{+6.67}_{-3.43})$	$(^{+6.3}_{-9.1})$	(0.001)	(0.001)	(0.2)	(0.003)	
B3	1.96	1.88	74.2	218.3	15.2	83.0	−0.12	35.3	−0.007	0.005	4969.0	0.962	2.004
						NGC 4261							
C1	1.67	1.62	60.8	−20.5	40.6	⋯	⋯	⋯	0.069	0.021	2207.0	1.050	1.263
	(0.10)	$(^{+0.46}_{-0.40})$	$(^{+2.8}_{-3.3})$	$(^{+2.0}_{-1.9})$	(6.1)				(0.007)	(0.008)	$(^{+5.6}_{-5.5})$	(0.032)	
C2	1.68	1.77	60.6	−20.8	40.1	⋯	⋯	⋯	0.070	0.023	2205.6	1.049	1.263
D	1.55	1.90	60.8*	−15.5	0.0	162.4	⋯	72.2	0.053	0.017	2218.9	1.118	1.199
E	1.47	2.18	60.8*	−17.9	35.6	⋯	⋯	⋯	0.040	0.036	2207.0*	1.102	1.491

Note. Best-fit parameter values obtained by fitting the models described in Table 2 to the CO (2−1) and CO (3−2) data cubes. Parameter values followed by "*" were held fixed. For NGC 315, Υ is the J-band stellar mass-to-light ratio; for NGC 4261, Υ refers to the H-band mass-to-light ratio. The major-axis PA Γ is measured east of north to the receding side of the disk. The disk kinematic center (x_c, y_c) is given in terms of R.A. and decl. offsets from the nuclear continuum source centroid at $0^h57^m48\overset{s}{.}883$, $+30°21'08\overset{''}{.}81$ for NGC 315 and $12^h19^m23\overset{s}{.}216$, $+05°49'29\overset{''}{.}69$ for NGC 4261 (J2000). In these models, the disk systemic velocity $v_{\rm sys}$ is taken to be the recessional velocity $cz_{\rm obs}$ in the barycentric frame that is used to transform the models to observed frequency units. Statistical uncertainties for the model B2 and C1 parameters are given in parentheses and were determined using the 68% confidence intervals from Monte Carlo resampling.

4×4 pixel regions to create nearly beam-sized cells. From the final rebinned data cube, we measured the rms background in line-free areas in each channel and calculated the χ^2 statistic in a fitting region that fully encompasses the observed CO emission.

4.2. NGC 315 Modeling Results

We fit models to the NGC 315 CO (2−1) data cube over a region that is elliptical in each channel and extends across velocities of 4400−5420 km s^{-1} (roughly $|v_{\rm LOS} - v_{\rm sys}| \lesssim 550$ km s^{-1}). The spatial fitting region has a semimajor axis of $r_{\rm fit} = 1\overset{''}{.}60$, an axis ratio of $b/a = 0.26$, and a major-axis PA of 41°. After block-averaging data and model cubes, the fitting region contains 10,404 data points. We began by optimizing model A, which assumes a uniform $\sigma_{\rm turb}$ and employs the luminous mass model that was constructed after masking the most dust-obscured regions. The model A best-fit parameters are $M_{\rm BH} = 2.39 \times 10^9\ M_\odot$, $\Upsilon_J = 2.06\ M_\odot/L_\odot$, and $\sigma_1 = 15.3$ km s^{-1} (see Table 3 for the complete results). The total $\chi^2 = 21272.0$ and the number of degrees of freedom ($N_{\rm dof}$) is 10,395, which results in $\chi^2_\nu = \chi^2/N_{\rm dof} = 2.046$.

For scenario B1, we used the same luminous mass model as in model A, while for B2 and B3 we adopted each of the extinction-corrected MGEs in turn. Models B1−B3 also included the more general Gaussian $\sigma_{\rm turb}(r)$ prescription. Model B2 is the best match to the data, with $\chi^2 = 20705.1$ over $N_{\rm dof} = 10392$, so we adopted B2 and its best-fit $M_{\rm BH} = 2.08 \times 10^9\ M_\odot$ as the fiducial model. Model B2 is not formally an acceptable fit with $\chi^2_\nu = 1.992$; however, the first-moment map and PVD derived from the model B2 cube do match the observed CO kinematic behavior (Figure 7) apart from modest (±20 km s^{-1}) discrepancies near the kinematic center. For nearly the entire disk region (except for $R \lesssim 0\overset{''}{.}1$; Figure 8), the model line profiles closely follow the data. The best-fit $\Upsilon_J = 1.87\ M_\odot/L_\odot$ is below the expected $2.2 < \Upsilon_J < 2.8\ M_\odot/L_\odot$ for single stellar population (SSP) models that assume a Salpeter (1955) initial mass function (IMF) with old ages (∼10−14 Gyr) and solar metallicities, while the inferred $1.5 < \Upsilon_J < 1.9\ M_\odot/L_\odot$ from our dynamical model is above the expected Υ_J for a Kroupa (2001) or Chabrier (2003) IMF (Vazdekis et al. 2010).

Models B1 and B3 return $M_{\rm BH} = (1.96-2.40) \times 10^9\ M_\odot$ and $\Upsilon_J = (1.88-2.05)\ M_\odot/L_\odot$, with $\chi^2 = 20{,}829.9-21{,}155.5$. All the NGC 315 models prefer a low σ_1 of ∼15.3 km s^{-1}, which is consistent with many other spatially resolved ALMA CO observations of ETGs (e.g., Paper I; Ruffa et al. 2019a). If we use a Gaussian function for $\sigma_{\rm turb}$, the profile remains centrally peaked ($r_0 \sim 0$ pc) and concentrated ($\mu \lesssim 35$ pc), with $\sigma_0 \sim$ 85−150 km s^{-1}. Comparing models A and B1, the choice of a radially uniform versus a more flexible, centrally peaked $\sigma_{\rm turb}$ results in inconsequential changes to both $M_{\rm BH}$ and χ^2. For an even more edge-on disk in NGC 1332, Barth et al. (2016b) found a strong degeneracy between the σ_0 and $M_{\rm BH}$ parameters, concluding that beam-smearing effects were to blame. Subsequent gas-dynamical modeling of higher-resolution data did not demonstrate that $\sigma_{\rm turb}$ needs to be centrally and broadly peaked to reproduce CO kinematics (Barth et al. 2016a; Paper II).

The ∼20% difference in BH mass ($\Delta M_{\rm BH}$) between models B1 and B3 is driven by a more than order-of-magnitude increase in the central stellar luminosity density. We treat $\Delta M_{\rm BH}$ as representative of the systematic uncertainty introduced by circumnuclear dust. The $\Delta M_{\rm BH}$ arising from dust corrections is roughly twice as large as the BH mass range derived from similar gas-dynamical models of NGC 3258 from ALMA Cycle 2 CO (2−1) observations (with $A_H = 0-1.50$ mag; Paper II). The larger spread in BH masses for NGC 315 is the result of the disk's higher inclination angle and CO observations that do not extend as deeply within r_g.

In Figure 9, we show $\Delta\chi^2 = \chi^2 - \min(\chi^2)$ curves for models B1−B3. To construct the plots, we fixed the BH mass in each trial while allowing all other parameters to vary, and we recorded the χ^2 value from the best-fit model. The 1σ uncertainties derived from $\Delta\chi^2 < 1$ regimes are ∼0.2%, which are far smaller than the systematic uncertainties arising from plausible extinction corrections to the luminous mass model. Since block averaging does not fully eliminate noise correlations between neighboring pixels, we do not use $\Delta\chi^2$ to determine the $M_{\rm BH}$ statistical uncertainty. Instead, we carried out 300 Monte Carlo realizations using the resampling procedure introduced in Paper II. At each iteration, line-free slices (where $|v_{\rm LOS} - v_{\rm sys}| > 560$ km s^{-1}) were drawn

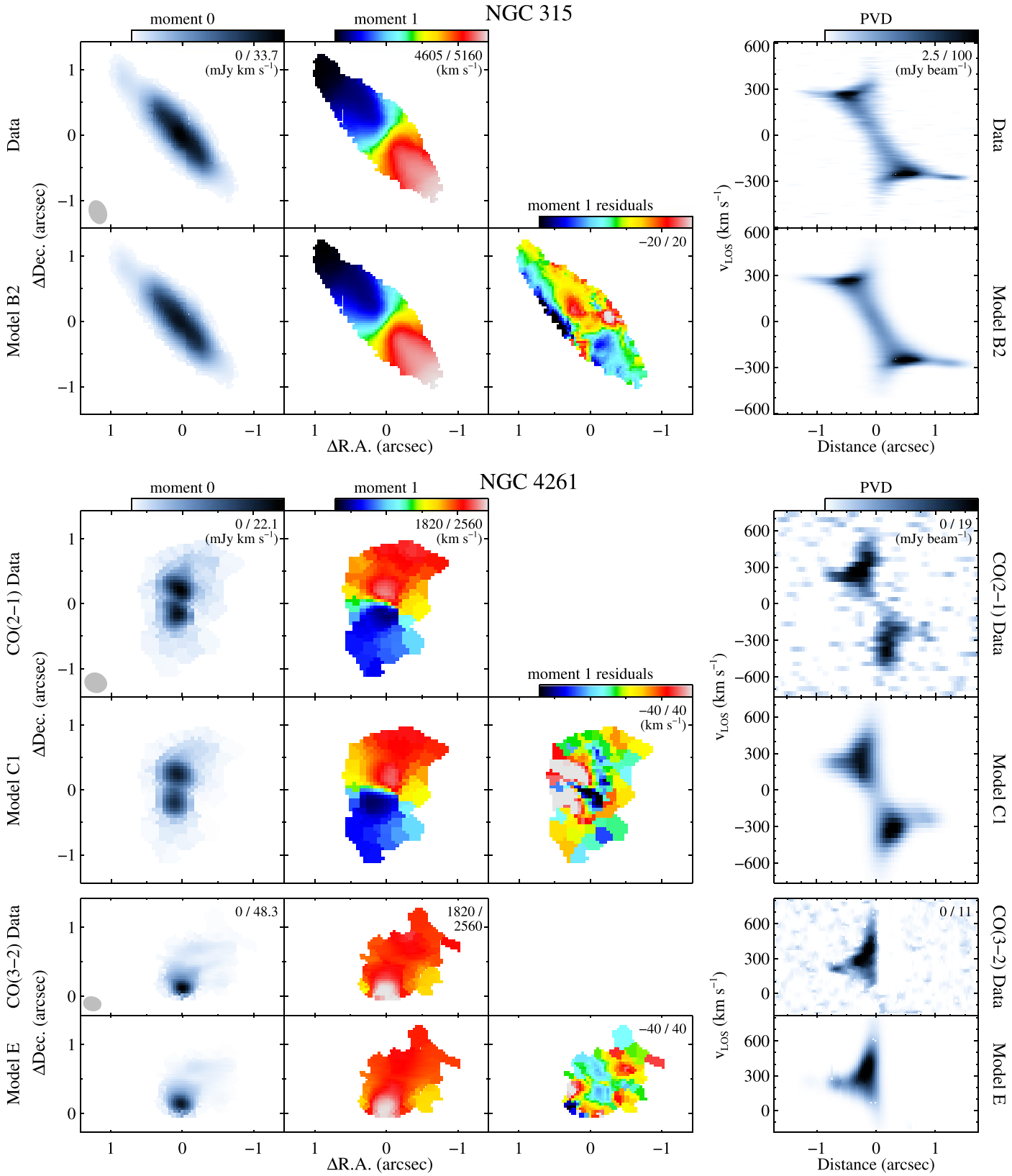

Figure 7. Comparison of the luminosity-weighted NGC 315 CO (2−1) (top panels) and NGC 4261 CO (2−1) and CO (3−2) (middle and bottom panels) zeroth- and first-moment maps and PVDs with those derived from best-fitting models B2, C1, and E. With the noticeable exception of model C1 for NGC 4261, the first-moment residual maps show generally small deviations ($\lesssim$10 km s^{-1}, or 4%) between data and the best-fit models, with the largest discrepancies near the disk center. Likewise, the model PVDs generally agree with the data. However, model B2 for NGC 315 underrepresents the CO (2−1) emission that has $|v_{\rm LOS} - v_{\rm sys}| \gtrsim 350$ km s^{-1}, and model C1 for NGC 4261 cannot reproduce the sharp velocity upturn seen in the approaching side of the disk.

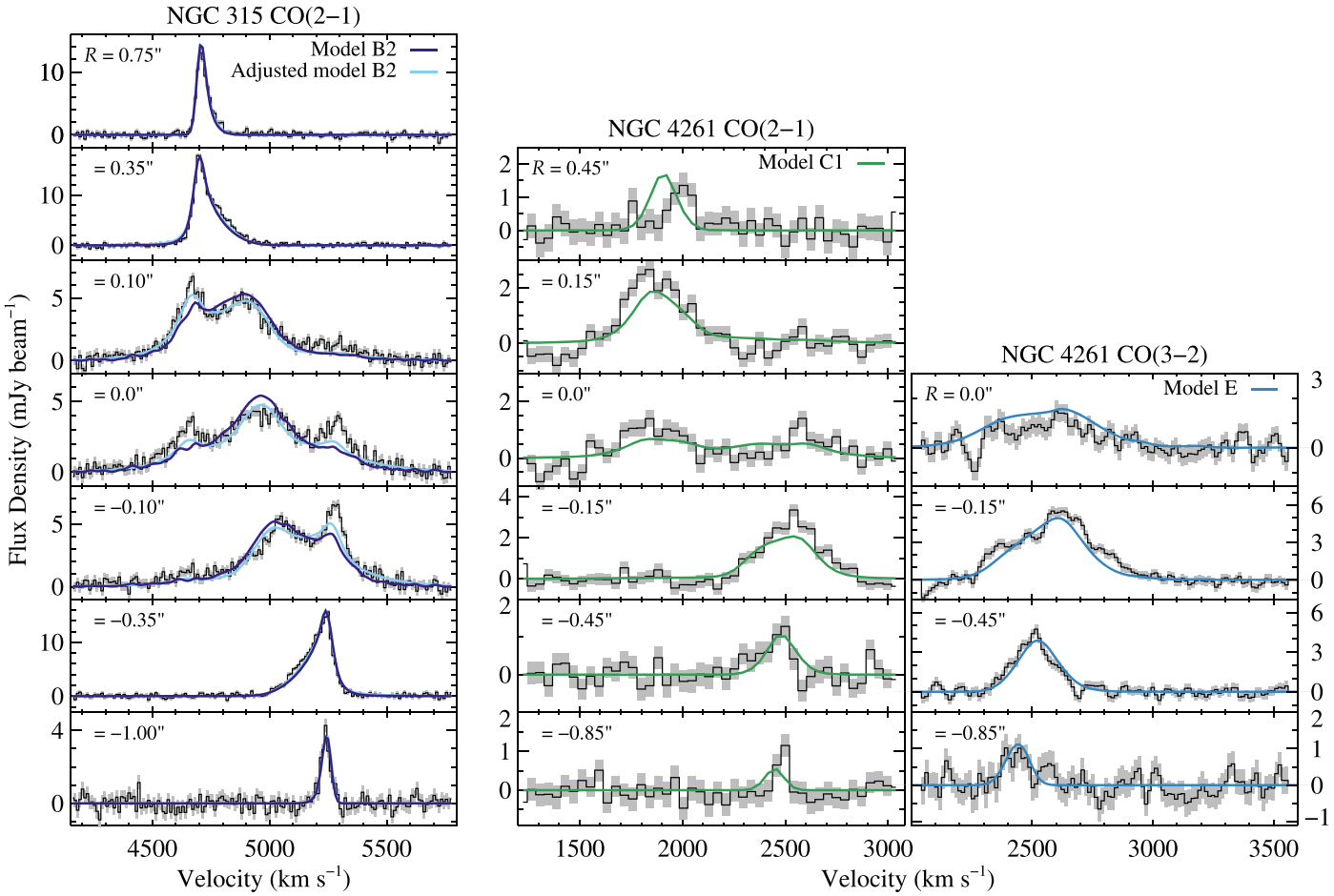

Figure 8. Comparison between Voronoi-binned line profiles extracted from both data and best-fit model cubes at select radii R from the kinematic center along the disk major axis. Positive R corresponds to the approaching side of the disk. Shaded regions indicate the frequency-dependent background rms. We adjusted the intrinsic flux map used in model B2 for NGC 315 and assigned larger CO flux within a central nuclear ring. The model line profiles are in better agreement with the data, and there is no change to $M_{\rm BH}$. For NGC 4261, the discrepancies between the CO (2−1) data and model C1 at large radii are primarily driven by kinematic twists in the outer disk. In the central ($R = 0\farcs0$) spectrum of the NGC 4261 CO (3−2) data cube, there may be an absorption feature at $v_{\rm LOS} \sim 2260$ km s^{-1}. Perhaps because of coarser channel binning, no absorption feature is apparent at the same location in the CO (2−1) data cube.

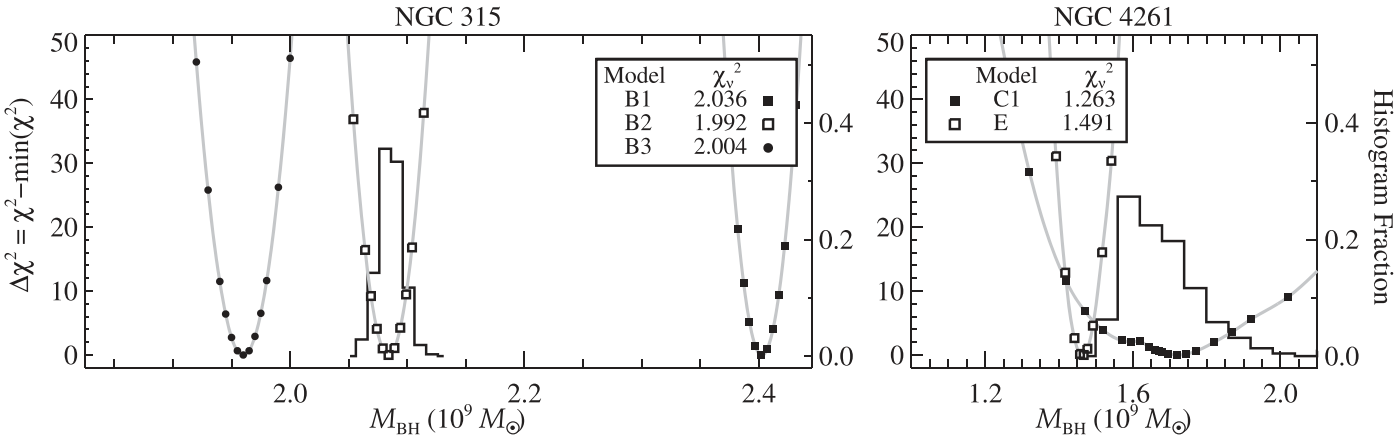

Figure 9. Results from χ^2 minimization as a function of BH mass for the NGC 315 CO (2−1) and NGC 4261 CO (2−1) and CO (3−2) dynamical models. Gray lines are spline interpolations to the $\Delta\chi^2 = \chi^2 - \min(\chi^2)$ values. The histograms show the distributions of BH masses determined from Monte Carlo resampling of the B2 and C1 best-fit model cubes.

from the CO (2−1) data cube and randomly added to the best-fit model B2 cube before optimization of all model parameters. From this suite of Monte Carlo realizations, we estimated 1σ uncertainties for each parameter by taking the 15.9 and 84.1 percentiles of the respective distributions. The final statistical $M_{\rm BH}$ uncertainty is $\sim 10^7$ $M_\odot$, or roughly 0.5% of the best-fit BH mass. The remaining parameter statistical uncertainties for model B2 are listed in Table 3. We expect the statistical uncertainties on the model B2 parameters to be representative of those for the B1 and B3 models.

In addition to calculating the $M_{\rm BH}$ statistical uncertainty and exploring the effect of dust, we ran additional tests to measure the $\Delta M_{\rm BH}$ that arises from other possible systematics. In each instance, we modified details of our model B2 to examine the impacts of various assumptions. These tests are described below.

Pixel oversampling.—Previous gas-dynamical modeling of resolved CO disks demonstrated little sensitivity to the choice of pixel oversampling (e.g., Barth et al. 2016b; Paper II). Nevertheless, we tested various factors from $s=1$ to $s=10$. The χ^2 decreased between $s=1$ and $s=2$, where $\chi^2_\nu = 1.904$, and then increased and plateaued at $\chi^2_\nu \approx 2.150$ for $s \geqslant 4$. For $s \geqslant 4$, $M_{\rm BH}$ converged to the model B2 value in Table 3, with less than a 0.1% scatter in the best-fit mass. Even without any pixel oversampling, the BH mass is only ∼1% removed from the fiducial $s=4$ run.

Deconvolution.—At larger radii the best-fit models reproduce the observed emission-line profiles very well. Closer to the nucleus, however, the nonunique deconvolution results in a nearly flat projected CO surface brightness, $\Sigma'_{\rm CO}$, that does not give sufficient weight to high $|v_{\rm LOS} - v_{\rm sys}|$ emission (see Figure 8). To explore the impact of an uncertain central CO distribution, we manually reassigned deconvolved flux in the $s=4$ oversampled map, concentrating flux from the central 100 pc region into a tight elliptical annulus concentrated at radii of ∼30−40 pc. After rebinning to the native pixel scale and convolving with the beam, we find that the reassignment conserves flux and visually appears almost identical to the observed $\Sigma'_{\rm CO}$. Using this adjusted flux map, the model fit returns a higher overall $\chi^2_\nu = 2.046$ but better reproduces line profiles for $R < 0\farcs1$ (see Figure 8). The resulting BH mass is lower by $\Delta M_{\rm BH} = -7.4 \times 10^7\ M_\odot$ (∼4% of $M_{\rm BH}$), consistent with studies that note that the choice of intrinsic flux map impacts the quality of the fit but has a small effect on the inferred $M_{\rm BH}$ (e.g., Marconi et al. 2006; Walsh et al. 2013).

Gas mass.—Models A−B3 ignore the $M_{\rm gas} \approx 2.3 \times 10^8\ M_\odot$ mass of the disk itself. We explored the impact on $M_{\rm BH}$ and Υ_J by including the contribution to the circular velocity due to the gas mass ($v_{\rm c,gas}$) in addition to the stellar contribution derived from the MGE. We measured the CO (2−1) surface brightness from the zeroth-moment map within elliptical annuli, determined the corresponding projected surface mass densities, and numerically integrated assuming a thin disk to calculate $v_{\rm c,gas}$. Throughout the disk, we found $v_{\rm c,gas} \lesssim 60$ km s^{-1}. Including the gas mass in our dynamical model produced no noticeable change in $M_{\rm BH}$, Υ_J, or the other parameters.

Radial motion.—While the bright, unresolved millimeter to radio continuum source and radio jet suggest an actively accreting nucleus in NGC 315, the regular CO kinematics give no indication of significant noncircular gas motion near the BH. Regardless, we followed the method outlined in Paper II to estimate the potential impact of radial motion and included a simple radial velocity term ($v_{\rm rad}$) to represent either bulk inflow or outflow. The radial velocity term is a free parameter that is projected along the line of sight and added directly to the $v_{\rm LOS}$ map. Although not fully self-consistent, this toy model provides an estimate of the amount of radial flow allowed by the data. After optimizing the model, we found a best-fit inflow speed of ∼11.4 km s^{-1} but a nearly identical inferred BH mass, within ∼0.3% of model B2, and a somewhat improved $\chi^2_\nu = 1.959$. Radial flows produce kinematic twists in otherwise regular velocity fields. A similar twist can also be caused by a warped disk, and so the minor preference for radial inflow may instead be due to a slight warp in the gas disk.

Final error budget.—As expected, the systematic uncertainties (sys) in the NGC 315 BH mass measurement are dominated by the uncertainty due to the dust correction. To this term, we added the remaining $\Delta M_{\rm BH}$ from the other systematic effects we explored in quadrature. Together with the statistical (stat) BH mass uncertainty estimated from Monte Carlo realizations, our final BH mass measurement with 1σ uncertainty ranges is $(M_{\rm BH}/10^9\ M_\odot) = 2.08 \pm 0.01({\rm stat})^{+0.32}_{-0.14}({\rm sys})$. Our quoted systematic error budget for NGC 315 is provisional given that our models do not provide a formally acceptable fit to the data. We have chosen not to examine ad hoc procedures to address this issue (e.g., degrading the data quality by inflating the error bars to achieve a reduced χ^2 of 1 and therefore a formally acceptable fit, or excluding portions of the data where the model fits are poor), and these issues will be mitigated by future (approved Cycle 7) higher-resolution data that will allow for a less model-dependent approach.

4.3. NGC 4261 Modeling Results

We optimized the thin-disk model C1 to the NGC 4261 CO (2−1) cube, with spatially uniform $\sigma_{\rm turb}$ and an MGE constructed from the dust-masked H-band image. This fit was made to an elliptical spatial region that is uniform across channels with velocities in the range 1585–2805 km s^{-1} (roughly $|v_{\rm LOS} - v_{\rm sys}| \lesssim 600$ km s^{-1}) with $r_{\rm fit} = 1\farcs00$, an axis ratio of $b/a = 0.42$, and a major-axis PA of −20°. After 4 × 4 block-averaging the data and model cubes, the fitting region contains 1178 data points. This model, with a best-fit BH mass of $1.67 \times 10^9\ M_\odot$, achieved $\chi^2 = 1476.7$ over $N_{\rm dof} = 1169$ for $\chi^2_\nu = 1.263$. The best-fit $\Upsilon_H = 1.62\ M_\odot/L_\odot$ is consistent with the expected H-band stellar mass-to-light ratios for old, solar-metallicity SSPs ranging between 1.02 and 1.84 $M_\odot/L_\odot$ depending on the IMF (Vazdekis et al. 2010).

The best-fit $i = 60\fdg8$ is slightly lower than the value estimated by Ferrarese et al. (1996), who used the outer dust disk b/a from the F547M–F791W color map to estimate $i \approx \cos^{-1}(b/a) = 64°$. They noted that the disk has different oblateness on the approaching and receding sides, so we extended their analysis by also fitting additional ellipses to the color contours on each side of the disk separately (Figure 10). Our full-disk fit returns $b/a = 0.42$, while $b/a = 0.38$ and 0.49 for the receding and approaching sides of the disk, respectively. The corresponding disk inclination angle is $(65\fdg3^{+2.1}_{-4.7})$, and we estimated a major-axis PA for the disk of $(-17\fdg2^{+2.1}_{-3.7})$. Our model C1 i and Γ appear consistent with the dust disk morphology and orientation.

The best-fit model first-moment map qualitatively agrees with the observed CO kinematic behavior at most locations, although discrepancies exceeding 40 km s^{-1} arise both near the nucleus and at the disk edge, as our thin-disk formalism does not allow for a changing disk PA with radius (see Figures 5 and 8). In Paper II, we examined a gas disk with a similar $\Delta\Gamma_{\rm LON} \sim 20°$ and demonstrated that accounting for a slight warp in the disk may introduce a shift in BH mass at the few percent level. The model C1 PVD does not fully capture the sharp central rise in CO (2−1) emission-line speeds, most noticeably on the approaching side of the disk. One plausible explanation is a rapid increase in disk inclination angle in the central ∼40 pc. A second possibility is a sudden rise in intrinsic line widths from ∼20 to over 100 km s^{-1} at the same radius.

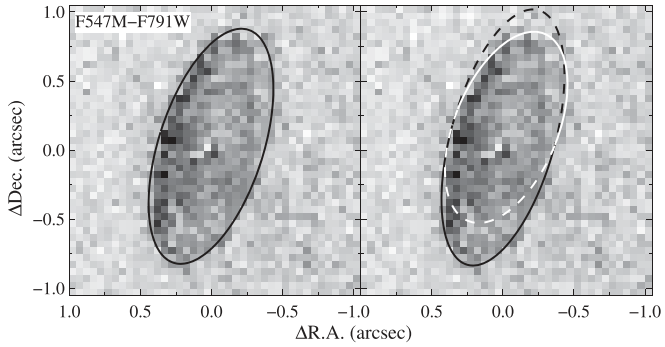

Figure 10. Central $2'' \times 2''$ region of the NGC 4261 F547M−F791W color map used to estimate the disk inclination angle. Superposed on the image are ellipses fit to color contours that trace the entire outer disk (left panel) and those fit to either the receding (white) or the approaching (black) side. The dashed lines show where the ellipses are extrapolated beyond the fitting regions.

The S/N of the NGC 4261 CO (2−1) data does not permit exploration of a more general disk structure, but we do test a more flexible $\sigma_{\rm turb}$ function in model D.

The model C1 $\Delta\chi^2$ as a function of BH mass (Figure 9) suggests a much larger statistical uncertainty compared to the NGC 315 results. As we increased the fixed $M_{\rm BH}$ above $\sim 1.8 \times 10^9\ M_\odot$, the best-fit i trended downward toward $\sim 55°$, resulting in a noticeably asymmetric $\Delta\chi^2$ curve. Following the NGC 315 approach, we estimated the NGC 4261 statistical uncertainty by carrying out 300 Monte Carlo realizations, randomly adding line-free channels of the CO (2−1) data cube to the best-fit model C1 cube. We determined the 1σ uncertainty for each parameter from the respective distributions (Table 3); the $M_{\rm BH}$ statistical uncertainty is $1.0 \times 10^8\ M_\odot$, or 6% of the model C1 BH mass. Notably, the statistical uncertainties for Υ_H and σ_1 are much larger, exceeding 25% and 15% of the respective best-fit values. Also, the statistical uncertainty on i ($\pm 3°$) is larger than typically seen with ALMA CO dynamical models, which is likely the result of our not having high-S/N CO emission over the full spatial extent of the disk.

Next, we employed the extinction-corrected ($A_H = 0.4$ mag) MGE in model C2. As demonstrated in Paper II and above for NGC 315, the uncertainty in the dust attenuation can be the dominant systematic of the BH mass error budget. However, the model C2 $\chi^2 = 1476.3$, which is essentially identical to that of model C1. The best-fit C2 model has $M_{\rm BH} = 1.68 \times 10^9\ M_\odot$ and $\Upsilon_H = 1.77\ M_\odot/L_\odot$, indicating that a "dust-corrected" stellar mass model has negligible impact on the best-fit parameters. The stark difference in $\Delta M_{\rm BH}$ for NGC 315 and NGC 4261 suggests that a larger portion of the NGC 4261 gas disk is within $r_{\rm g}$, and therefore the central CO kinematics are much less sensitive to the extended mass distribution.

We discussed above how the best-fit C1 model qualitatively agrees with the observed first-moment values at most locations, with the largest discrepancies occurring near the nucleus and the disk edge. In addition to these discrepancies, the model C1 best-fit σ_1 of 40.6 km s^{-1} results in model line profiles that are excessively broad near the disk edge. In model D, we relaxed the radially uniform constraint on intrinsic line widths by adopting an exponential function for $\sigma_{\rm turb}$. Early model D trials produced better fits with $\chi^2_\nu < 1.17$ and substantially higher (by at least 10%) $M_{\rm BH}$ and Υ_H. They also preferred disk inclination angles below 45°, which are highly inconsistent with the dust disk morphology and too low to allow for deprojection of the MGE. Closer inspection revealed a broad degeneracy between i and $M_{\rm BH}$. We thus fixed the model D i to the best-fit value from model C1 before optimizing the remaining free parameters. However, we note that the bulk of the CO emission is concentrated well within the outer edge of the dust disk that is used to estimate i (see Figure 5). Therefore, the dust morphology does not preclude a large decrease in i toward the disk center. For model D, the best-fit BH mass decreases to $1.55 \times 10^9\ M_\odot$ while Υ_H increases to $1.90\ M_\odot/L_\odot$. The $\sigma_{\rm turb}$ profile has $\mu = 72.2$ pc and line width amplitudes of $\sigma_0 = 162.4$ km s^{-1} and $\sigma_1 = 0.0$ km s^{-1}. At the disk edge, $\sigma_{\rm turb} \sim 20$ km s^{-1}, which is in closer agreement with the observed line widths than the uniform σ_1 value found for models C1−C2. Even though model D is a better fit to the CO (2−1) data with $\chi^2 = 1400.4$, because i is not a free parameter we elected to retain model C1 as our fiducial gas-dynamical model for NGC 4261. As a final note, the model D best-fit $v_{\rm sys}$ is 12 km s^{-1} larger than the model C1 value. The shift is likely due to the combination of the coarse channel spacing, the different line width prescription, and low S/N in the outer disk.

We investigated the stability of our CO (2−1) gas-dynamical modeling results by fitting the CO (3−2) data cube with thin-disk model E, which is analogous to model C1. Since the frequency coverage of the CO (3−2) data excludes most of the approaching side of the disk, we cannot constrain the systemic velocity, and we fixed this parameter to the best-fit $v_{\rm sys}$ from model C1. The spatial ellipse of the fitting region remains the same as for the CO (2−1) models, but we adopt a smaller velocity range of 2035−2920 km s^{-1} to calculate χ^2. After 4×4 block-averaging the data and model cubes, the fitting region contains 5280 data points. Like model D, early runs of model E showed a preference for very low i values, so we also fixed the disk inclination to the model C1 value. Optimizing all remaining free parameters gives $M_{\rm BH} = 1.47 \times 10^9\ M_\odot$, $\Upsilon_H = 2.18\ M_\odot/L_\odot$, and $\sigma_1 = 35.6$ km s^{-1}, with a total $\chi^2 = 7863.0$ over $N_{\rm dof} = 5273$ for $\chi^2_\nu = 1.491$. In Figure 7, we compare CO (3−2) moment maps and the PVD constructed from the best-fit model E with those drawn from the data cube. Line profiles extracted from the best-fit cube show good agreement with the data (Figure 8). Because model E adopts a fixed i, the curve of $\Delta\chi^2$ as a function of $M_{\rm BH}$ is narrow and symmetrical (Figure 9).

The range of BH mass measurements found from models C1−E of $(1.47-1.68) \times 10^9\ M_\odot$ reflects a few fundamental differences in model construction. The following paragraphs describe additional tests performed to probe other sources of systematic uncertainty when modeling the NGC 4261 CO (2−1) data cube. In each instance below, we modified aspects of our model C1 to estimate the impact of each systematic effect on the best-fit $M_{\rm BH}$.

Pixel oversampling.—As was the case for NGC 315, our NGC 4261 dynamical models converge to essentially the same BH masses when we adopt an oversampling of $s \geqslant 4$. For $s = 1$, the inferred BH mass is $\Delta M_{\rm BH} = -2.0 \times 10^8\ M_\odot$ compared to the fiducial value with a lower corresponding $\chi^2_\nu = 1.241$. With increasing oversampling, χ^2_ν increases until reaching a plateau at $s \geqslant 6$ with $\chi^2_\nu \approx 1.285$. For $s \geqslant 4$, we found a scatter of $2.1 \times 10^7\ M_\odot$ ($\sim 1.5\%$) in BH mass.

Block averaging.—The decision to 4×4 block-average data and model cubes before calculating χ^2 mitigates noise correlation between spatial pixels at the expense of spatial sampling. For the CO (2−1) data, our approach leaves fewer than 10 points per slice for $R < 0\farcs5$. However, within $0\farcs5$ the highest-S/N CO emission

and the most distinct Keplerian rotation signature are found. When the block averaging step is instead skipped, fits to the native data cube converged on a similar $M_{\rm BH}$ of $1.74 \times 10^9\ M_\odot$, corresponding to $\Delta M_{\rm BH} = 7.0 \times 10^7\ M_\odot$ or a 4% increase from the best-fit model C1 value. Our choice of block averaging size thus did not significantly bias the BH mass measurement.

Disk inclination.—The best-fit $i = 60\overset{\circ}{.}8$ from model C1 is at the lower end of the confidence interval $60\overset{\circ}{.}6-67\overset{\circ}{.}4$ derived from the morphology of the dust disk. Given the large estimate for the statistical uncertainty in the inclination angle, we ran a test with a fixed $i = 67\overset{\circ}{.}4$ that is at the high end of the likely inclination angles. In this case, the BH mass was higher by $3.7 \times 10^8\ M_\odot$ (or ∼22%).

Radial motion.—The slightly disturbed CO kinematics and irregular dust disk morphology may signal nonnegligible radial gas motion in the NGC 4261 disk. Introducing a bulk radial flow term $v_{\rm rad}$ as was done for NGC 315, we found a slight preference for an outflow with $v_{\rm rad} \sim 25$ km s^{-1}, which is only ∼10% of the observed CO $v_{\rm LOS}$ at the disk edge. Compared to model C1, the χ^2 and the best-fit $M_{\rm BH}$ increase by 6.7 and $5.5 \times 10^6\ M_\odot$, respectively. We note that the preference for $v_{\rm rad} \neq 0$ km s^{-1} is in part driven by tension between our axisymmetric thin-disk model and the observed CO kinematic twists.

Fitting region.—By applying `kinemetry` to the CO (2−1) first-moment map, we found that $\Delta\Gamma_{\rm LON} = 13°$ from the disk center to the edge. To determine the potential impact on $M_{\rm BH}$ of the moderate kinematic twist, we ran a test that restricted $r_{\rm fit}$ to $0\overset{''}{.}55$. Within this fitting region, the `kinemetry` results suggest that the gas is in simple, thin-disk rotation with $\Delta\Gamma_{\rm LON} < 3°$. Data within the smaller $r_{\rm fit}$ are insensitive to the extended stellar mass contributions, so we fixed Υ_H to the model C1 value. With only 10 data points per channel and no high-S/N CO detections that lie off the major axis, the inclination angle also needed to be fixed to $60\overset{\circ}{.}8$. When using the more central fitting region, we find that the best-fit BH mass increases by $\Delta M_{\rm BH} = 8.0 \times 10^7\ M_\odot$ or ∼5%.

Final error budget.—The largest positive and negative systematics for the NGC 4261 ALMA CO gas-dynamical models are the 22% increase in BH mass when adopting the upper-bound inclination angle and the 12% decrease when changing from CO (2−1) to CO (3−2) kinematic modeling. While not necessarily independent, we included the remaining systematic terms using a quadrature sum. Our final BH mass with 1σ statistical uncertainties is $\log_{10}(M_{\rm BH}/10^9\ M_\odot) = 1.67 \pm 0.10({\rm stat})^{+0.39}_{-0.24}({\rm sys})$.

5. Discussion

From ALMA observations of rotating circumnuclear molecular gas disks in the active galaxies NGC 315 and NGC 4261, we infer the presence of BHs with respective masses of $2.08 \times 10^9\ M_\odot$ and $1.67 \times 10^9\ M_\odot$. Our work provides the first dynamical measurement of the BH in NGC 315 and significantly improves on a prior ionized gas-dynamical $M_{\rm BH}$ determination for NGC 4261 (Ferrarese et al. 1996). Both galaxies were observed as part of our ongoing program to take an accurate census of BHs in massive ETGs by exploiting ALMA's unique capabilities. In the cases of NGC 315 and NGC 4261, we obtain ∼10%–25% precision on $M_{\rm BH}$, with the final error budgets being dominated by modeling systematics. Below we compare our determinations to other BH mass estimates and discuss how well the ALMA observations resolve the NGC 315 and NGC 4261 BH spheres of influence, possible future improvements to the $M_{\rm BH}$ measurements, and prospects for inferring BH masses in active galaxies with ALMA.

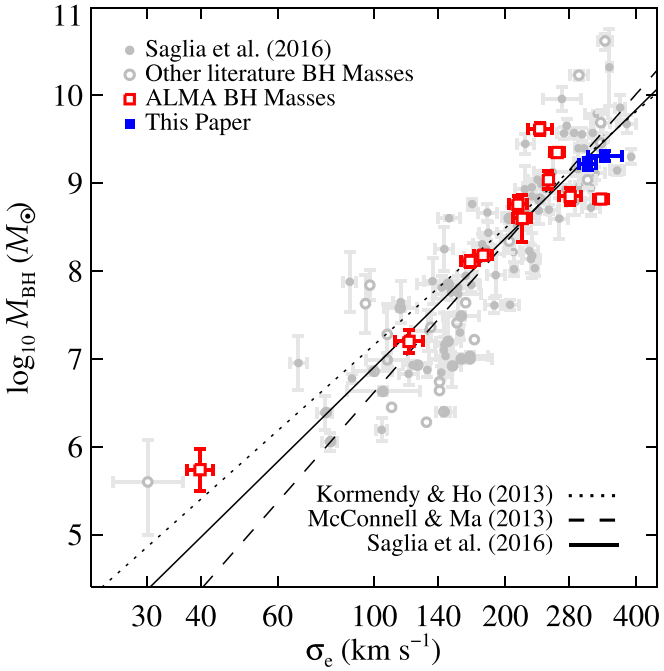

Figure 11. Comparison between dynamically measured BH masses and host galaxy $\sigma_{\rm e}$ (filled gray circles; Saglia et al. 2016), along with other literature values (open gray circles; den Brok et al. 2015; Greene et al. 2016; Thomas et al. 2016; Walsh et al. 2016, 2017; Erwin et al. 2018; Krajnović et al. 2018; Mehrgan et al. 2019; Liepold et al. 2020) and those measured using ALMA observations (colored squares; Barth et al. 2016a; Davis et al. 2017, 2018, 2020; Onishi et al. 2017; Boizelle et al. 2019; Nagai et al. 2019; North et al. 2019; Ruffa et al. 2019a; Smith et al. 2019; Nguyen et al. 2020). When not listed in the papers, we adopted $\sigma_{\rm e}$ values and/or uncertainties when available from other sources (Barth et al. 2002; Filippenko & Ho 2003; Brough et al. 2007; Cappellari et al. 2013; Kormendy & Ho 2013; Ma et al. 2014; Saglia et al. 2016; van den Bosch 2016; Veale et al. 2017). The NGC 315 and NGC 4261 BH masses presented here are consistent with $M_{\rm BH}$–$\sigma_{\rm e}$ relations from Kormendy & Ho (2013), McConnell & Ma (2013), and Saglia et al. (2016).

5.1. BH Mass

Using the stellar velocity dispersion measured within the galaxy effective radius ($\sigma_{\rm e}$) for NGC 315 of 341 km s^{-1} (Veale et al. 2017), the $M_{\rm BH}$–$\sigma_\star$ relation (Kormendy & Ho 2013; McConnell & Ma 2013; Saglia et al. 2016) predicts BH masses in the range of $(3.2-3.9) \times 10^9\ M_\odot$ (Figure 11), where we have adopted the fit to elliptical galaxies and classical bulges from Kormendy & Ho (2013) and Saglia et al. (2016) and the fit to early-type galaxies from McConnell & Ma (2013). Likewise, the expected $M_{\rm BH}$ for NGC 4261, with $\sigma_{\rm e} = 315$ km s^{-1} (Kormendy & Ho 2013), is $(2.2-2.7) \times 10^9\ M_\odot$. Our dynamical $M_{\rm BH}$ measurements for both galaxies are below the mean values predicted from the $M_{\rm BH}$–$\sigma_\star$ relation but are within the intrinsic scatter of the relation. Even if we assume a smaller stellar velocity dispersion of $\sigma_{\rm e} = 265$ km s^{-1} for NGC 4261 (Cappellari et al. 2013), our dynamical $M_{\rm BH}$ remains consistent with the $M_{\rm BH}$–$\sigma_\star$ relation.

In order to compare to the $M_{\rm BH}$–$L_{\rm bul}$ relation (Kormendy & Ho 2013), we used the MGE models in Table 1 and assumed colors of $J-K = 0.9$ mag and $H-K = 0.2$ mag for an old, solar-metallicity SSP (Vazdekis et al. 2010). We found $L_{{\rm bul},K} = 8.9 \times 10^{11}\ L_\odot$ for NGC 315 and $1.3 \times 10^{11}\ L_\odot$ for NGC 4261,

corresponding to predicted BH masses of $7.8 \times 10^9\ M_\odot$ and $0.72 \times 10^9\ M_\odot$, respectively. If instead we used the total apparent K-band magnitude from the HyperLeda database (Makarov et al. 2014) for NGC 315, then $L_{\mathrm{bul},K} = 6.8 \times 10^{11}\ L_\odot$, which translates to $M_{\mathrm{BH}} = 5.7 \times 10^9\ M_\odot$. The $L_{\mathrm{bul},K}$ estimated from our MGE model for NGC 4261 agrees with the HyperLeda value. Thus, our NGC 315 gas-dynamical M_{BH} is an outlier, lying below the lower envelope of BH masses populating the M_{BH}–L_{bul} relation, while our ALMA-based M_{BH} for NGC 4261 is consistent with the M_{BH}–L_{bul} correlation.

We also estimated the bulge mass by multiplying the J- and H-band total luminosities from the MGEs in Table 1 by Υ_J from model B2 for NGC 315 and by Υ_H from model C1 for NGC 4261. This estimate resulted in a bulge mass of $1.2 \times 10^{12}\ M_\odot$ for NGC 315, a predicted $M_{\mathrm{BH}} = (3.2\text{–}3.9) \times 10^9\ M_\odot$ from McConnell & Ma (2013) and Saglia et al. (2016), and $M_{\mathrm{BH}} = 9.0 \times 10^9\ M_\odot$ from Kormendy & Ho (2013). For NGC 4261, we found a bulge mass of $3.8 \times 10^{11}\ M_\odot$ and an expected $M_{\mathrm{BH}} = (1.2\text{–}2.3) \times 10^9\ M_\odot$ (Kormendy & Ho 2013; McConnell & Ma 2013; Saglia et al. 2016). Our NGC 315 BH mass is consistent within the intrinsic scatter of the M_{BH}–M_{bul} relation (McConnell & Ma 2013; Saglia et al. 2016) but lies well below the predicted value using the M_{BH}–M_{bul} relation from Kormendy & Ho (2013), although the large uncertainty in the galaxy distance limits the significance of the discrepancy. Our NGC 4261 BH mass is consistent with all of the M_{BH}–M_{bul} relations.

At present, there is not another dynamical mass measurement for the NGC 315 BH. However, Beifiori et al. (2009) estimated a rough BH mass upper limit by fitting a rotating disk model to the central [N II] line width, which was measured from a single spectrum extracted from an HST Space Telescope Imaging Spectrograph (STIS) observation. They neglected the stellar contribution to the gravitational potential and did not consider the effects of dynamically significant turbulent motion. Assuming an inclination angle of 81° and 33°, they found M_{BH} upper limits of $(0.5\text{–}2.0) \times 10^9\ M_\odot$ (scaled to our adopted distance). While the STIS data appear to support a conclusion of rotation (Noel-Storr et al. 2003), the ionized gas kinematics are sufficiently chaotic to remove any tension with our ALMA-derived BH mass. Possible future stellar-dynamical modeling of this galaxy (Ma et al. 2014; Ene et al. 2019) may enable a meaningful direct comparison between a precision ALMA CO BH mass and a stellar-dynamical BH mass measurement (e.g., Krajnović et al. 2009; Rusli et al. 2011; Schulze & Gebhardt 2011; Barth et al. 2016a; Davis et al. 2017; Smith et al. 2019).

In contrast to NGC 315, the mass of the central BH in NGC 4261 has been previously measured using ionized gas. Ferrarese et al. (1996) conducted one of the earliest gas-dynamical BH studies with HST, and the measurement was used to establish the original M_{BH}–$\sigma_\star$ relation, along with a small handful of other targets (Gebhardt et al. 2000; Ferrarese & Merritt 2000). Ferrarese et al. (1996) derived gas kinematics from 13 nuclear spectra obtained with the HST Faint Object Spectrograph (FOS) and modeled the radial velocities assuming a purely Keplerian potential. They found a BH mass of $(5.0 \pm 1.0) \times 10^8\ M_\odot$ (scaled to our distance). Although our ALMA gas-dynamical M_{BH} is inconsistent with Ferrarese et al. (1996), we employed a much more sophisticated and detailed dynamical model using methods that have been developed over the past two decades. In particular, the ionized gas-dynamical modeling did not account for PSF blurring, which is expected to yield an underestimate of the BH mass. Also, Kormendy & Ho (2013) argue that some of the BH masses based on ionized gas, including NGC 4261, were likely underestimated because of nongravitational gas perturbations. The ALMA data further provide substantial advantages over the FOS observations, including better spatial coverage of the gas disk and a focus on a well-defined, isolated CO emission line. We note that Humphrey et al. (2009) estimated a BH mass that was consistent with Ferrarese et al. (1996) by modeling the hot interstellar medium of NGC 4261, assuming that the X-ray-emitting gas is in hydrostatic equilibrium. However, tension with our M_{BH} suggests that the hot plasma near the AGN is strongly affected by nongravitational motions.

5.2. Resolving the BH Sphere of Influence

The precision of a BH mass measurement is in large part determined by how well the BH sphere of influence is resolved. In Paper II, we detected CO (2–1) down to radii of $\sim 0.14 r_{\mathrm{g}}$ in NGC 3258. The ALMA data had a relative resolution of $\xi = 2r_{\mathrm{g}}/\theta_{\mathrm{FWHM}} \sim 17$ and facilitated an M_{BH} measurement with percent-level precision. A relative resolution of $\xi \sim 17$ is typical of very long baseline interferometry observations of megamaser galaxies (e.g., Kuo et al. 2011; Zhao et al. 2018). Although a few similar cases exist (Nagai et al. 2019; North et al. 2019; Smith et al. 2019), most published ALMA CO data sets of circumnuclear disks are obtained with $\xi \lesssim 2$ (e.g., Davis et al. 2017, 2018; Boizelle et al. 2017; Onishi et al. 2017; Ruffa et al. 2019b; Zabel et al. 2019; Nguyen et al. 2020). This limitation leads to larger uncertainty in the BH mass measurement, often driven by various systematic effects. In addition, spatial blurring in highly inclined disks entangles minor-axis ($v_{\mathrm{LOS}} \sim v_{\mathrm{sys}}$) emission with the highest $|v_{\mathrm{LOS}} - v_{\mathrm{sys}}|$ emission near the nucleus (Barth et al. 2016b). In order to evaluate how well the data resolve r_{g}, one should also consider the relative resolution of r_{g} along the projected minor axis, or if $\xi \cos i \gtrsim 2$ (Barth et al. 2016b). To date, only three ALMA CO observations meet this criterion and detect emission deep within the BH-dominated region (Nagai et al. 2019; Paper II; North et al. 2019).

For the NGC 315 CO (2–1) data, we directly calculated r_{g} for models A–B3 by finding the radius where the various luminous mass contributions to v_{c} equal that from the BH. We find that r_{g} ranges between 0.″67 and 0.″80 with CO emission detected down to $\sim(0.11\text{–}0.14) r_{\mathrm{g}}$. This result corresponds to a high ξ of ~ 5 but only a marginally resolved $\xi \cos i$ of ~ 1.4. For NGC 4261, models C1–E suggest $r_{\mathrm{g}} = 1.''24\text{–}1.''58$, which extends beyond the disk edge. We detected CO down to radii of $\sim(0.06\text{–}0.08) r_{\mathrm{g}}$. With $\xi \sim 9.6$ and $\xi \cos i$ of about 4.9, the current CO data fully resolve the BH sphere of influence.

The dominant systematic in the NGC 315 measurement is the uncertainty in the luminous mass model due to the presence of nuclear dust. Using different MGE models with various levels of extinction correction leads to a ∼6%–15% uncertainty in M_{BH}. This exercise highlights the need to carefully consider the effects of dust in situations where the ALMA observations only marginally resolve r_{g}. For NGC 315, r_{g} is well resolved along the major axis but not well resolved along the projected minor axis. We expect the systematic uncertainty due to dust to be even more severe for cases where r_{g} along the major axis is also not well resolved. Higher angular resolution CO imaging of NGC 315, approved in an ALMA Cycle 7 program, will fully isolate the locus of rapid gas rotation within r_{g} and allow for the extended stellar mass distribution to be constrained directly from the CO emission-line kinematics, as

was done in Paper II. Such an approach will eliminate the primary modeling systematic and will permit an $M_{\rm BH}$ determination with percent-level precision. Based on the Cycle 6 observations presented in this paper, we expect CO imaging with a similar line sensitivity of 0.2 mJy beam^{-1} per 20 km s^{-1} channel, and a resolution of $0\farcs1$ will allow for a direct determination of the extended mass distribution and a resulting high-precision measurement of the BH mass.

The ALMA observations of NGC 4261 highly resolve $r_{\rm g}$ along both the major and minor axes, and the CO (2−1) and CO (3−2) kinematics clearly show Keplerian features. However, the lower S/N of the CO disk leads to degeneracies between $M_{\rm BH}$, i, and $\sigma_{\rm turb}$. Moreover, there are indications that the CO disk is mildly warped with a kinematic PA that varies by $\sim15^\circ$ over the disk. The NGC 4261 CO kinematics are less affected by dust correction errors than those for NGC 315. Since the CO emission in NGC 4261 probes deeper within $r_{\rm g}$, we expect follow-up observations at $\sim$0.17 mJy beam^{-1} per 20 km s^{-1} channel, and $\theta_{\rm FWHM} \lesssim 0\farcs15$ would facilitate more robust dynamical models that account for the disk's warped structure and intrinsic line widths and would yield a very precise $M_{\rm BH}$ determination.

5.3. BH Mass Measurement Prospects for Radio-loud Galaxies with ALMA

Including the two galaxies presented here, ALMA observations have resolved CO emission in at least 11 FR I ETGs (Boizelle et al. 2017; Nagai et al. 2019; North et al. 2019; Rose et al. 2019; Ruffa et al. 2019a, 2019b; Vila-Vilaro et al. 2019). NGC 4261 and two other FR I galaxies show central CO emission deficits, with the $\Sigma'_{\rm CO}$ of the other two tracing large (kiloparsec-scale) rings. The CO emission in the remaining eight FR I galaxies is centrally concentrated in disks with outer radii of $\lesssim$500 pc. Central CO emission is not detected at circular speeds above 700 km s^{-1} for any FR I galaxy observed to date, which suggests that the CO-emitting gas is absent or faint within about 10−30 pc of the BH (for more discussion, see Davis et al. 2019; Paper II). However, these radio-loud ETGs are expected to have large $r_{\rm g}$ of $\sim$50−250 pc assuming the current BH−host galaxy relations, and over half of the ALMA CO data sets show at least some evidence for Keplerian-like gas rotation.

Nearly all of the 11 radio-loud galaxies with CO emission detected by ALMA host dust disks. In one exception (IC 1459; Ruffa et al. 2019b), filamentary dust is not accompanied by CO emission, and in another case (NGC 1275; Nagai et al. 2019), the bright nucleus may obscure circumnuclear dust features. Other studies have highlighted the tendency for ETGs with nuclear radio emission to contain dust disks (e.g., Tran et al. 2001; Nyland et al. 2016), further suggesting a link between the formation of dust disks and AGNs. For example, previous HST surveys detected dust near the centers of about half of all nearby radio-loud galaxies (e.g., van Dokkum & Franx 1995; Martel et al. 1999; Verdoes Kleijn et al. 1999), roughly the same as the fraction in radio-quiet ETGs (e.g., Ebneter & Balick 1985; Ebneter et al. 1988; van Dokkum & Franx 1995; Tomita et al. 2000; Tran et al. 2001; Lauer et al. 2005).

Taken together, the large expected $r_{\rm g}$ and the high prevalence of dust/molecular gas disks make FR I galaxies compelling candidates for precision BH mass measurements. It is worth noting, however, that for galaxies with the brightest compact millimeter/submillimeter continua ($S_{\rm nuc} \gtrsim 1$ Jy; e.g., Nagai et al. 2019), the spectral dynamic range resulting from calibration and deconvolution errors can limit the faintest detectable emission-line features. Also, CO absorption is sometimes observed against the nuclear continuum (e.g., Boizelle et al. 2017; Nagai et al. 2019; Rose et al. 2019; Ruffa et al. 2019b) and could dilute emission features. On the plus side, the presence of bright (>50 mJy) nuclear millimeter/submillimeter emission allows for a better phase solution using continuum self-calibration, and CO line imaging with $\theta_{\rm FWHM} \lesssim r_{\rm g}$ can help to disentangle emission and absorption while unambiguously isolating rapid central emission arising from well within $r_{\rm g}$.

6. Conclusion

We present the first dynamical BH mass measurement for NGC 315 and a much improved $M_{\rm BH}$ determination for NGC 4261 based on ALMA $\sim0\farcs2$−$0\farcs3$ resolution CO imaging. With the NGC 315 CO (2−1) and NGC 4261 CO (2−1) and CO (3−2) data, we examined the spatial and kinematic structure of the arcsecond-scale circumnuclear disks. We detected CO emission well within the BH-dominated region of the galaxies and traced Keplerian-like rotation down to just 15−30 pc (or $\sim$0.1 $r_{\rm g}$) from their BHs. Using thin-disk gas-dynamical models, we inferred BH masses of 2.08×10^9 $M_\odot$ for NGC 315 and 1.67×10^9 $M_\odot$ for NGC 4261, which are generally consistent with the predictions from the BH−host galaxy relations. In the case of NGC 4261, we have revised the prior ionized gas-dynamical $M_{\rm BH}$ measurement (Ferrarese et al. 1996) upward by a factor of $\sim$3.

We explored statistical uncertainties and various sources of systematic errors to establish BH mass confidence intervals. In both galaxies, the molecular gas is accompanied by significant dust that obscures the stellar light at the center of even near-IR HST images. For the highly inclined disk in NGC 315, we estimated a central dust extinction of $A_J \lesssim 1.50$ mag and constructed luminous mass models that bracket the range of likely stellar surface brightness distributions. Adopting the various luminous mass models when fitting gas-dynamical models to the ALMA data cube resulted in a change of $\sim$15% in $M_{\rm BH}$. Dust has a smaller impact on our estimate of $M_{\rm BH}$ for NGC 4261, and we found a negligible change in $M_{\rm BH}$ when using a luminous mass model with a greater central stellar luminosity density. Instead, the NGC 4261 $M_{\rm BH}$ is affected at the $\sim$10%−25% level by degeneracies with the inclination angle, the turbulent gas velocity dispersion, and the systemic velocity, which arise owing to a mildly warped CO disk observed at moderately low S/N. We also found a $\sim$10% change in $M_{\rm BH}$ when modeling CO (3−2) ALMA data across half the disk. Ultimately, we determined a statistical uncertainty of 0.5% and a systematic uncertainty of 7%–15% in $M_{\rm BH}$ for NGC 315 and a 6% statistical uncertainty and a 14%–23% systematic uncertainty in $M_{\rm BH}$ for NGC 4261. Although not considered in this paper, we note that uncertainties in the galaxy distances introduce an additional systematic to each BH mass error budget that is commensurate with the respective distance uncertainty.

Our work adds to the rapidly growing number of molecular gas-dynamical $M_{\rm BH}$ determinations from ALMA. With this new method of $M_{\rm BH}$ measurement, we are able to consistently obtain precise masses, at the 10%−20% level or below, in nearby ETGs, including those that reside at the currently sparsely populated upper end of the $M_{\rm BH}$−$\sigma_\star$, $M_{\rm BH}$−$L_{\rm bul}$, and

$M_{BH}-M_{bul}$ correlations. The observed NGC 315 and NGC 4261 CO kinematics warrant even higher angular resolution (and, for NGC 4261, higher-S/N) imaging with ALMA to fully map v_{LOS} within r_g, which should enable exceptionally robust BH mass measurements free from the dominant systematics we explore here. Taking an accurate census of BHs across a wide variety of galaxies is essential to understanding the role of BHs in galaxy evolution, and percent-level M_{BH} precision will enable a more thorough exploration of accretion processes for these active galaxies.

Based on observations with the NASA/ESA Hubble Space Telescope obtained at the Space Telescope Science Institute, which is operated by the Association of Universities for Research in Astronomy, Incorporated, under NASA contract NAS5-26555. Support for program No. 15909 was provided through a grant from the STScI under NASA contract NAS5-26555. J.L.W. was supported in part by NSF grant AST-1814799. Research at UC Irvine was supported by NSF grant AST-1614212. L.C.H. was supported by the National Science Foundation of China (11721303, 11991052) and the National Key R&D Program of China (2016YFA0400702). This paper makes use of the following ALMA data: ADS/JAO.ALMA#2017.1.00301.S and ADS/JAO.ALMA#2017.1.01638.S. ALMA is a partnership of ESO (representing its member states), NSF (USA), and NINS (Japan), together with NRC (Canada), MOST and ASIAA (Taiwan), and KASI (Republic of Korea), in cooperation with the Republic of Chile. The Joint ALMA Observatory is operated by ESO, AUI/NRAO, and NAOJ. The National Radio Astronomy Observatory is a facility of the National Science Foundation operated under cooperative agreement by Associated Universities, Inc. The work has made use of the NASA/IPAC InfraRed Science Archive, which is funded by NASA and operated by the California Institute of Technology.

Software: AstroDrizzle (Gonzaga et al. 2012), TweakReg (Gonzaga et al. 2012), GALFIT (Peng et al. 2002, 2010), IRAF (Tody 1986, 1993), CASA (v5.1.2; McMullin et al. 2007).

Appendix

In Table A1 we list the best-fit parameters of the "dust-corrected" MGEs for NGC 315 and NGC 4261. Details of the dust correction and MGE construction are provided in Section 2.4.

Table A1
Dust-corrected MGE Parameters

j (1)	$\log_{10} I_{J,j}$ ($L_\odot$ pc^{-2}) (2)	σ'_j (arcsec) (3)	q'_j (4)	$\log_{10} I_{J,j}$ ($L_\odot$ pc^{-2}) (5)	σ'_j (arcsec) (6)	q'_j (7)	$\log_{10} I_{H,j}$ ($L_\odot$ pc^{-2}) (8)	σ'_j (arcsec) (9)	q'_j (10)
	NGC 315						NGC 4261		
	$A_J = 0.75$ mag			$A_J = 1.50$ mag			$A_H = 0.40$ mag		
1	3.924	0.178	0.764	4.407	0.119	0.787	5.219	0.017	0.650
2	3.896	0.617	0.716	3.912	0.644	0.681	1.753	0.102	0.650
3	3.899	1.292	0.777	3.891	1.294	0.781	4.357	1.257	0.787
4	3.459	2.414	0.706	3.457	2.409	0.705	4.152	2.801	0.724
5	3.474	4.159	0.722	3.476	4.152	0.722	3.667	5.222	0.710
6	3.014	8.211	0.663	3.015	8.206	0.663	3.369	9.995	0.765
7	2.844	13.26	0.748	2.844	13.26	0.748	3.034	16.74	0.844
8	2.072	26.50	0.765	2.073	26.49	0.763	2.409	37.29	0.817
9	2.164	30.83	0.689	2.164	30.84	0.690	2.059	65.12	0.901
10	1.839*	61.95*	0.810*	1.839*	61.95*	0.810*	0.914*	144.4*	0.820*
11	0.939*	192.6*	0.980*	0.939*	192.6*	0.980*	...	...	...

Note. NGC 315 and NGC 4261 MGE solutions constructed from their respective HST J- and H-band mosaics. For NGC 315, the model has a uniform PA $= 44.^\circ31$ for all components, while the best-fit NGC 4261 MGE has PA $= -22.^\circ03$. Column (1) lists the component number, Column (2) is the central surface brightness assuming absolute solar magnitudes of $M_{\odot,J} = 3.82$ mag and $M_{\odot,H} = 3.37$ mag (Willmer 2018), Column (3) gives the Gaussian standard deviation along the major axis, and Column (4) provides the component axis ratio. Primes indicate projected quantities. Spitzer IRAC1 MGE components, identified with an asterisk, were included as fixed components when an MGE was fit to the HST image. When constructing the NGC 315 MGE, we modeled the AGN as a point source (with $m_J = 19.2$ mag); likewise, the NGC 4261 MGE was accompanied by an unresolved nuclear source (with $m_H = 19.6$ mag).

ORCID iDs

Benjamin D. Boizelle https://orcid.org/0000-0001-6301-570X
Jonelle L. Walsh https://orcid.org/0000-0002-1881-5908
Aaron J. Barth https://orcid.org/0000-0002-3026-0562
David A. Buote https://orcid.org/0000-0002-3202-9487
Andrew J. Baker https://orcid.org/0000-0002-7892-396X
Jeremy Darling https://orcid.org/0000-0003-2511-2060
Luis C. Ho https://orcid.org/0000-0001-6947-5846
Jonathan Cohn https://orcid.org/0000-0003-1420-6037
Kyle M. Kabasares https://orcid.org/0000-0003-2632-8875

References

Alatalo, K., Davis, T. A., Bureau, M., et al. 2013, MNRAS, 432, 1796
Barth, A. J., Boizelle, B. D., Darling, J., et al. 2016a, ApJL, 822, L28
Barth, A. J., Darling, J., Baker, A. J., et al. 2016b, ApJ, 823, 51
Barth, A. J., Ho, L. C., & Sargent, W. L. W. 2002, AJ, 124, 2607
Barth, A. J., Sarzi, M., Rix, H.-W., et al. 2001, ApJ, 555, 685
Beifiori, A., Sarzi, M., Corsini, E. M., et al. 2009, ApJ, 692, 856
Bernardi, M., Hyde, J. B., Sheth, R. K., Miller, C. J., & Nichol, R. C. 2007, AJ, 133, 1741
Bogdán, Á., Lovisari, L., Volonteri, M., & Dubois, Y. 2018, ApJ, 852, 131
Boizelle, B. D., Barth, A. J., Darling, J., et al. 2017, ApJ, 845, 170
Boizelle, B. D., Barth, A. J., Walsh, J. L., et al. 2019, ApJ, 881, 10
Briggs, D. S. 1995, BAAS, 27, 1444
Brough, S., Proctor, R., Forbes, D. A., et al. 2007, MNRAS, 378, 1507
Cappellari, M. 2002, MNRAS, 333, 400
Cappellari, M., & Copin, Y. 2003, MNRAS, 342, 345
Cappellari, M., Emsellem, E., Krajnović, D., et al. 2011, MNRAS, 413, 813
Cappellari, M., Scott, N., Alatalo, K., et al. 2013, MNRAS, 432, 1709
Carilli, C. L., & Walter, F. 2013, ARA&A, 51, 105
Chabrier, G. 2003, PASP, 115, 763
Combes, F., Young, L. M., & Bureau, M. 2007, MNRAS, 377, 1795
Crook, A. C., Huchra, J. P., Martimbeau, N., et al. 2007, ApJ, 655, 790
Davies, R. L., & Birkinshaw, M. 1986, ApJL, 303, L45
Davis, D. S., Mushotzky, R. F., Mulchaey, J. S., et al. 1995, ApJ, 444, 582
Davis, T. A., Bureau, M., Cappellari, M., Sarzi, M., & Blitz, L. 2013, Natur, 494, 328
Davis, T. A., Bureau, M., Onishi, K., et al. 2017, MNRAS, 468, 4675
Davis, T. A., Bureau, M., Onishi, K., et al. 2018, MNRAS, 473, 3818
Davis, T. A., Greene, J. E., Ma, C.-P., et al. 2019, MNRAS, 486, 1404
Davis, T. A., Nguyen, D. D., Seth, A. C., et al. 2020, MNRAS, 496, 4061
de Vaucouleurs, G., de Vaucouleurs, A., Corwin, H. G., Jr, et al. 1991, Third Reference Catalogue of Bright Galaxies (New York: Springer), 2091
den Brok, M., Seth, A. C., Barth, A. J., et al. 2015, ApJ, 809, 101
Dressel, L. 2019, Wide Field Camera 3 Instrument Handbook (Baltimore, MD: STScI), https://hst-docs.stsci.edu/wfc3ihb
Ebneter, K., & Balick, B. 1985, AJ, 90, 183
Ebneter, K., Djorgovski, S., & Davis, M. 1988, AJ, 95, 422
Ene, I., Ma, C.-P., McConnell, N. J., et al. 2019, ApJ, 878, 57
Ene, I., Ma, C.-P., Walsh, J. L., et al. 2020, ApJ, 891, 65
Ensslin, T. A., Simon, P., Biermann, P. L., et al. 2001, ApJL, 549, L39
Erwin, P., Thomas, J., Saglia, R. P., et al. 2018, MNRAS, 473, 2251
Faber, S. M., Tremaine, S., Ajhar, E. A., et al. 1997, AJ, 114, 1771
Faesi, C. M., Lada, C. J., & Forbrich, J. 2018, ApJ, 857, 19
Fazio, G. G., Hora, J. L., Allen, L. E., et al. 2004, ApJS, 154, 10
Ferrarese, L., Ford, H. C., & Jaffe, W. 1996, ApJ, 470, 444
Ferrarese, L., & Merritt, D. 2000, ApJL, 539, L9
Filippenko, A. V., & Ho, L. C. 2003, ApJL, 588, L13
Fomalont, E., van Kempen, T., Kneissl, R., et al. 2014, Msngr, 155, 19
Gebhardt, K., Bender, R., Bower, G., et al. 2000, ApJL, 539, L13
Gonzaga, S., Hack, W., Fruchter, A., & Mack, J. 2012, The DrizzlePac Handbook (Baltimore, MD: STScI), http://drizzlepac.stsci.edu
Goudfrooij, P., de Jong, T., Hansen, L., & Norgaard-Nielsen, H. U. 1994, MNRAS, 271, 833
Goullaud, C. F., Jensen, J. B., Blakeslee, J. P., et al. 2018, ApJ, 856, 11
Greene, J. E., Seth, A., Kim, M., et al. 2016, ApJL, 826, L32
Gu, Q. S., Huang, J. S., Wilson, G., & Fazio, G. G. 2007, ApJL, 671, L105
Güver, T., & Özel, F. 2009, MNRAS, 400, 2050
Ho, L. C., Filippenko, A. V., & Sargent, W. L. W. 1997, ApJS, 112, 315
Hoffmann, W. F., Hora, J. L., Mentzell, J. E., et al. 2004, Proc. SPIE, 5487, 186
Holtzman, J. A., Burrows, C. J., Casertano, S., et al. 1995, PASP, 107, 1065
Huchra, J. P., Macri, L. M., Masters, K. L., et al. 2012, ApJS, 199, 26
Humphrey, P. J., Buote, D. A., Brighenti, F., Gebhardt, K., & Mathews, W. G. 2009, ApJ, 703, 1257
Jaffe, W., Ford, H., Ferrarese, L., van den Bosch, F., & O'Connell, R. W. 1996, ApJ, 460, 214
Jaffe, W., & McNamara, B. R. 1994, ApJ, 434, 110
Jones, D. L., & Wehrle, A. E. 1997, ApJ, 484, 186
Kennedy, R., Bamford, S. P., Häußler, B., et al. 2016, A&A, 593, A84
Kormendy, J., & Ho, L. C. 2013, ARA&A, 51, 511
Kormendy, J., & Richstone, D. 1995, ARA&A, 33, 581
Krajnović, D., Emsellem, E., Cappellari, M., et al. 2011, MNRAS, 414, 2923
Krajnović, D., Cappellari, M., McDermid, R. M., et al. 2018, MNRAS, 477, 3030
Krajnović, D., McDermid, R. M., Cappellari, M., & Davies, R. L. 2009, MNRAS, 399, 1839
Krist, J., & Hook, R. 2004, The Tiny Tim User's Guide (Baltimore, MD: STScI), http://www.stsci.edu/hst/observatory/focus/TinyTim
Kroupa, P. 2001, MNRAS, 322, 231
Kuo, C. Y., Braatz, J. A., Condon, J. J., et al. 2011, ApJ, 727, 20
La Barbera, F., De Carvalho, R. R., De La Rosa, I. G., et al. 2010, AJ, 140, 1528
Laing, R. A., Canvin, J. R., Cotton, W. D., & Bridle, A. H. 2006, MNRAS, 368, 48
Lauer, T. R., Ajhar, E. A., Byun, Y. I., et al. 1995, AJ, 110, 2622
Lauer, T. R., Faber, S. M., Gebhardt, K., et al. 2005, AJ, 129, 2138
Lauer, T. R., Faber, S. M., Richstone, D., et al. 2007, ApJ, 662, 808
Liepold, C. M., Quenneville, M. E., Ma, C.-P., et al. 2020, ApJ, 891, 4
Lister, M. L., Aller, M. F., Aller, H. D., et al. 2018, ApJS, 234, 12
Lucy, L. B. 1974, AJ, 79, 745
Ma, C.-P., Greene, J. E., McConnell, N., et al. 2014, ApJ, 795, 158
Makarov, D., Prugniel, P., Terekhova, N., Courtois, H., & Vauglin, I. 2014, A&A, 570, A13
Marconi, A., Pastorini, G., Pacini, F., et al. 2006, A&A, 448, 921
Martel, A. R., Baum, S. A., Sparks, W. B., et al. 1999, ApJS, 122, 81
Mathis, J. S. 1990, ARA&A, 28, 37
McConnell, N. J., & Ma, C.-P. 2013, ApJ, 764, 184
McMullin, J. P., Waters, B., Schiebel, D., Young, W., & Golap, K. 2007, in ASP Conf. Ser. 376, Astronomical Data Analysis Software and Systems XVI, ed. R. A. Shaw, F. Hill, & D. J. Bell (San Francisco, CA: ASP), 127
Mehrgan, K., Thomas, J., Saglia, R., et al. 2019, ApJ, 887, 195
Nagai, H., Onishi, K., Kawakatu, N., et al. 2019, ApJ, 883, 193
Nguyen, D. D., den Brok, M., Seth, A. C., et al. 2020, ApJ, 892, 68
Noel-Storr, J., Baum, S. A., Verdoes Kleijn, G., et al. 2003, ApJS, 148, 419
Nolthenius, R. 1993, ApJS, 85, 1
North, E. V., Davis, T. A., Bureau, M., et al. 2019, MNRAS, 490, 319
Nyland, K., Young, L. M., Wrobel, J. M., et al. 2016, MNRAS, 458, 2221
Ocaña Flaquer, B., Leon, S., Combes, F., & Lim, J. 2010, A&A, 518, A9
Onishi, K., Iguchi, S., Davis, T. A., et al. 2017, MNRAS, 468, 4663
Onishi, K., Iguchi, S., Sheth, K., & Kohno, K. 2015, ApJ, 806, 39
Peng, C. Y., Ho, L. C., Impey, C. D., & Rix, H.-W. 2002, AJ, 124, 266
Peng, C. Y., Ho, L. C., Impey, C. D., & Rix, H.-W. 2010, AJ, 139, 2097
Pirzkal, N. 2014, The Near Infrared Sky Background, Technical Report WFC3 ISR 2014-11
Planck Collaboration, Ade, P. A. R., Aghanim, N., et al. 2016, A&A, 594, A13
Press, W. H., Teukolsky, S. A., Vetterling, W. T., & Flannery, B. P. 1992, Numerical recipes in FORTRAN. The Art of Scientific Computing (Cambridge: Cambridge Univ. Press)
Richardson, W. H. 1972, JOSA, 62, 55
Rose, T., Edge, A. C., Combes, F., et al. 2019, MNRAS, 485, 229
Ruffa, I., Davis, T. A., Prandoni, I., et al. 2019a, MNRAS, 489, 3739
Ruffa, I., Prandoni, I., Laing, R. A., et al. 2019b, MNRAS, 484, 4239
Rusli, S. P., Thomas, J., Erwin, P., et al. 2011, MNRAS, 410, 1223
Saglia, R. P., Opitsch, M., Erwin, P., et al. 2016, ApJ, 818, 47
Salpeter, E. E. 1955, ApJ, 121, 161
Sandstrom, K. M., Leroy, A. K., Walter, F., et al. 2013, ApJ, 777, 5
Schlafly, E. F., & Finkbeiner, D. P. 2011, ApJ, 737, 103
Schulze, A., & Gebhardt, K. 2011, ApJ, 729, 21
Smith, M. D., Bureau, M., Davis, T. A., et al. 2019, MNRAS, 485, 4359
Thomas, J., Ma, C.-P., McConnell, N. J., et al. 2016, Natur, 532, 340
Tody, D. 1986, Proc. SPIE, 627, 733
Tody, D. 1993, in ASP Conf. Ser. 52, Astronomical Data Analysis Software and Systems II, ed. R. J. Hanisch, R. J. V. Brissenden, & J. Barnes (San Francisco, CA: ASP), 173
Tomita, A., Aoki, K., Watanabe, M., Takata, T., & Ichikawa, S.-I. 2000, AJ, 120, 123
Tonry, J. L., Dressler, A., Blakeslee, J. P., et al. 2001, ApJ, 546, 681

Tran, H. D., Tsvetanov, Z., Ford, H. C., et al. 2001, AJ, 121, 2928
Utomo, D., Blitz, L., Davis, T., et al. 2015, ApJ, 803, 16
van den Bosch, R. C. E. 2016, ApJ, 831, 134
van den Bosch, R. C. E., Greene, J. E., Braatz, J. A., Constantin, A., & Kuo, C.-Y. 2016, ApJ, 819, 11
van Dokkum, P. G., & Franx, M. 1995, AJ, 110, 2027
Vazdekis, A., Sánchez-Blázquez, P., Falcón-Barroso, J., et al. 2010, MNRAS, 404, 1639
Veale, M., Ma, C.-P., Thomas, J., et al. 2017, MNRAS, 464, 356
Venturi, T., Giovannini, G., Feretti, L., Comoretto, G., & Wehrle, A. E. 1993, ApJ, 408, 81
Verdoes Kleijn, G. A., Baum, S. A., de Zeeuw, P. T., & O'Dea, C. P. 1999, AJ, 118, 2592
Verdoes Kleijn, G. A., van der Marel, R. P., Carollo, C. M., & de Zeeuw, P. T. 2000, AJ, 120, 1221
Verdoes Kleijn, G. A., van der Marel, R. P., & Noel-Storr, J. 2006, AJ, 131, 1961
Viaene, S., Sarzi, M., Baes, M., Fritz, J., & Puerari, I. 2017, MNRAS, 472, 1286
Vila-Vilaro, B., Espada, D., Cortes, P., et al. 2019, ApJ, 870, 39
Walsh, J. L., Barth, A. J., Ho, L. C., & Sarzi, M. 2013, ApJ, 770, 86
Walsh, J. L., Barth, A. J., & Sarzi, M. 2010, ApJ, 721, 762
Walsh, J. L., van den Bosch, R. C. E., Gebhardt, K., et al. 2016, ApJ, 817, 2
Walsh, J. L., van den Bosch, R. C. E., Gebhardt, K., et al. 2017, ApJ, 835, 208
Willmer, C. N. A. 2018, ApJS, 236, 47
Worrall, D. M., Birkinshaw, M., Laing, R. A., Cotton, W. D., & Bridle, A. H. 2007, MNRAS, 380, 2
Young, L. M., Bureau, M., Davis, T. A., et al. 2011, MNRAS, 414, 940
Zabel, N., Davis, T. A., Smith, M. W. L., et al. 2019, MNRAS, 483, 2251
Zhao, W., Braatz, J. A., Condon, J. J., et al. 2018, ApJ, 854, 124